TUDelft

Delft University of Technology

Statistically optimal estimation of degree-1 and C_{20} coefficients based on GRACE data and an ocean bottom pressure model

Sun, Yu; Ditmar, Pavel; Riva, Riccardo

Important note
To cite this publication, please use the final published version (if applicable).
Please check the document version above.

Statistically optimal estimation of degree-1 and C_{20} coefficients based on GRACE data and an ocean bottom pressure model

Yu Sun, Pavel Ditmar and Riccardo Riva

Department of Geoscience and Remote Sensing, Delft University of Technology Stevinweg 1, 2628 *CN Delft, The Netherlands. E-mail: y.sun-2@tudelft.nl*

SUMMARY

In this study, we develop a methodology to estimate monthly variations in degree-1 and C_{20} coefficients by combing Gravity Recovery and Climate Experiment (GRACE) data with oceanic mass anomalies (combination approach). With respect to the method by Swenson *et al.*, the proposed approach exploits noise covariance information of both input data sets and thus produces stochastically optimal solutions supplied with realistic error information. Numerical simulations show that the quality of degree-1 and -2 coefficients may be increased in this way by about 30 per cent in terms of RMS error. We also proved that the proposed approach can be reduced to the approach of Sun *et al.* provided that the GRACE data are noise-free and noise in oceanic data is white. Subsequently, we evaluate the quality of the resulting degree-1 and C_{20} coefficients by estimating mass anomaly time-series within carefully selected validation areas, where mass transport is small. Our validation shows that, compared to selected Satellite Laser Ranging (SLR) and joint inversion degree-1 solutions, the proposed combination approach better complements GRACE solutions. The annual amplitude of the SLR-based C_{10} is probably overestimated by about 1 mm. The performance of the C_{20} coefficients, on the other hand, is similar to that of traditionally used solution from the SLR technique.

Key words: Satellite geodesy; Satellite gravity; Reference systems; Geopotential theory; Time variable gravity; Global change from geodesy.

1 INTRODUCTION

Since its launch in 2002, the Gravity Recovery and Climate Experiment (GRACE; Tapley *et al.* 2004) satellite mission allows data processing centres to produce monthly gravity field solutions (e.g. Bettadpur 2012; Watkins 2012; Dahle *et al.* 2013; Klinger & Mayer-Gürr 2016; Farahani *et al.* 2017). After subtracting a static/mean gravity field, the obtained time variations in the Earth's gravity field reflect changes in its mass distribution. Apart from the gravity changes originated from the interior of the solid Earth, such as those due to the Glacial Isostatic Adjustment (GIA) and megathrust earthquakes, the observed signals are caused by mass variations within a very thin layer enveloping the solid Earth (oceans, continental water/ice/snow storage, etc.). Using GRACE data as input, one can uniquely estimate the latter mass variations, which are of great interest in many applications, including the study of ongoing climate change.

Typically, a monthly GRACE gravity field solution is expressed by a set of spherical harmonic coefficients (SHCs) complete to a certain degree. One problem of these solutions is that they lack degree-1 coefficients (ΔC_{10}, ΔC_{11} and ΔS_{11}; the symbol Δ is dropped hereafter for simplicity), which are proportional to the geocentre motion defined as the displacement of centre of mass of the whole Earth system (CM) with respect to the centre of figure of the solid Earth (CF) (Ray 1999). Omission of the degree-1 contribution leads to significant errors in surface mass estimates (Wu *et al.* 2012). Another problem of GRACE monthly solutions is that the C_{20} coefficient is subject to large uncertainties (Chen *et al.* 2016), presumably due to thermal-related systematic errors in the accelerometer data (Cheng & Ries 2017). Therefore, for the purpose of inferring surface mass anomalies, a GRACE user is advised to complement GRACE solutions with independently estimated degree-1 coefficients and replace the native GRACE C_{20} coefficients with more accurate ones.

Most of studies published until now have been using the degree-1 coefficients as supplied by Swenson *et al.* (2008) (GRACE-OBP-Swenson), while the C_{20} coefficients are taken from Satellite Laser Ranging (SLR) analysis (Cheng *et al.* 2013a). This approach, however, has some weak points. First, the estimates of the degree-1 coefficients are not statistically optimal in the sense that errors in both GRACE data and the Ocean Bottom Pressure (OBP) model are not accounted for, as explained below. Second, the C_{20} coefficients produced from a different observation technique and with a different data processing procedure may not be consistent with GRACE solutions. As far as the degree-1 coefficients are concerned, the estimates provided with Swenson's approach are not optimal in a statistical sense.

The GRACE-OBP-Swenson approach estimates degree-1 coefficients by combining GRACE data and oceanic degree-1 coefficients extracted from an OBP model. In its original implementation, this approach yields a much smaller annual amplitude of the C_{10}

(~2 mm) than alternative techniques, such as SLR (~3 to ~6 mm) (e.g. Cheng *et al.* 2013b; Ries 2013; Sośnica *et al.* 2013) and GPS-based inversion (~3 to ~4 mm) (e.g. Wu *et al.* 2006; Jansen *et al.* 2009; Rietbroek *et al.* 2012). Sun *et al.* (2016a,b) developed an improved variant of the GRACE-OBP-Swenson approach (GRACE-OBP-Improved approach) by making a proper truncation of the input GRACE solutions, reducing GRACE signal leakage and taking into account self-attraction and loading (SAL) effects (Gordeev *et al.* 1977; Conrad & Hager 1997). The resulting C_{10} annual amplitude was about 3 mm, that is, in line with the GPS inversion method, as well as at least some of the SLR results. In addition, C_{20} time-series estimated this way compared well with several SLR-based solutions (e.g. Cheng *et al.* 2013a; Lemoine *et al.* 2013).

However, the underlying assumption of the GRACE-OBP-Improved method is the same as that of the GRACE-OBP-Swenson method: that the degree-1 and C_{20} from an OBP models as well as GRACE data are treated deterministically, which implies that these data are free of error. As a consequence, any errors in OBP modelling and GRACE data propagate into degree-1 and C_{20} estimates in an uncontrolled way, that is, the estimation procedure is statistically not optimal.

With this study, we propose to modify the GRACE-OBP approach in such a way that degree-1 and C_{20} coefficients are estimated by means of a statistically optimal combination of GRACE data and an OBP model (the combination approach). Furthermore, a realistic estimation of uncertainties in the input data is part of the combination approach, which allows us to supply the estimated low-degree coefficients with a stochastic description of their errors.

The combination approach can also be considered as a variant of the joint inversion procedure (Rietbroek *et al.* 2009, 2012), developed as an effort to improve global GPS inversions. In these studies, surface loading variations (up to a maximum degree of 30) were estimated from a combination of GPS, GRACE, and OBP data. As a result, the degree-1 information comes from GPS-derived degree-1 mass loading and the OBP data. However, the GPS tracking network is highly uneven and sometimes very sparse, which may lead to a prominent network effect. Also, it is still challenging to isolate a load-induced contribution from the total GPS site movements (Dong *et al.* 2002). In addition, the deficiency in modelling/removing the draconitic error in GPS data processing (Griffiths & Ray 2013) adds further uncertainty to GPS-sensed degree-1 information. Another problem of the above procedure is that the three data sets are not coupled. For example, total ocean mass is conserved, and water exchange with continents is not taken into account. In this study, the GPS data are not used. Furthermore, total ocean masses are coupled with surface mass changes over land.

It goes without saying that correcting GRACE solutions with accurate estimates of degree-1 and C_{20} coefficients improves the mass anomaly estimates. Still, it is important to quantify such improvements and to compare the obtained mass anomaly estimates with those based on the traditionally used degree-1 and C_{20} coefficients. Therefore, in this study we also propose a method to evaluate the quality of the obtained degree-1 and C_{20} coefficients in terms of inferred surface mass anomalies.

The paper is organized as follows. We describe the combination approach in details in Section 2. Then, we conduct numerical experiments to verify the correctness of the approach as well as to identify its optimal implementation parameters (Section 4). Afterwards, we apply the selected parameter setting to derive degree-1 and C_{20} time-series using real data (Section 5). We then demonstrate that using these coefficients improves the estimates of regional mass variations (Section 6). Finally, Section 7 concludes the paper.

2 METHODOLOGY

2.1 Combination approach

Various data sets can be combined in the statistically optimal sense if their noise variance–covariance matrices are available (a general form of the optimal data combination is presented in Appendix A). The optimal data combination in the context of the GRACE-OBP-Improved approach is presented below.

Let the mass anomaly (in terms of equivalent water height) at a point k be denoted as h_k. The oceanic mass anomaly function can then be expressed as a linear combination of surface spherical harmonics:

$$h_k = \vartheta_k \sum_{l=1}^{\infty} \sum_{m=-l}^{l} C_{lm}^{(h)} Y_{lm,k}, \tag{1}$$

where ϑ_k represents the ocean function, which equals 1 if k is a point over ocean and equals 0 otherwise; $Y_{lm,k}$ is the normalized surface spherical harmonic of degree l and order m at point k; $C_{lm}^{(h)}$ are the spherical harmonic coefficients describing surface mass re-distribution. These coefficients are called thereafter mass coefficients. Note that summation in eq. (1) starts from degree 1, which implies a conservation of total mass. Also note that the summation is truncated at a certain degree in practice. Eq. (1) can be re-written in terms of matrix-to-vector multiplication as

$$\mathbf{h} = \mathbf{OYd}, \tag{2}$$

where $\mathbf{h}$ is the $K \times 1$ vector of mass anomalies h_k, with K the number of grid points; $\mathbf{Y}$ is the $K \times L$ matrix with entries equal to $Y_{lm,k}$; $\mathbf{d}$ is the $L \times 1$ vector containing coefficients $C_{lm}^{(h)}$ starting from degree 1, with L the number of mass coefficients, and $\mathbf{O}$ is a $K \times K$ diagonal matrix with elements representing the ocean function, that is,

$$\{\mathbf{O}\}_{(k,k)} = \begin{cases} 1 & \text{if } k \text{ is a point in ocean} \\ 0 & \text{if } k \text{ is a point on land.} \end{cases} \tag{3}$$

Assuming that mass redistribution takes place in a thin spherical layer, we can relate the mass coefficients to the dimensionless SHCs, according to Wahr *et al.* (1998)

$$\mathbf{d} = \mathbf{Sx}, \tag{4}$$

where $\mathbf{x}$ is the $L \times 1$ vector containing the set of dimensionless SHCs. $\mathbf{S}$ is the $L \times L$ diagonal matrix with entries

$$\{\mathbf{S}\}_{(lm,lm)} = \frac{(2l+1)}{3(1+k_l)} \frac{\rho_{\text{earth}}}{\rho_{\text{water}}} a, \tag{5}$$

where a is the Earth's average radius; ρ_{earth} is the average density of the Earth, ρ_{water} is the density of water and k_l is the load Love number of degree l. Note that $k_1 = 0.021$ (which is slightly dependent on the chosen Earth model), which implies that the vector x in eq. (4) should be provided in the CF frame (Blewitt 2003).

Therefore, our functional model is

$$\begin{cases} \mathbf{Tx} = \mathbf{x}_g \\ \mathbf{OYSx} = \mathbf{h}, \end{cases} \tag{6}$$

where $\mathbf{x}_g$ is a $L_g \times 1$ vector containing the SHCs provided by GRACE, L_g equals $(L - 4)$ since we assume that degree-1 and C_{20}

coefficients are absent; **T** is a truncated unit matrix of size $L_g \times L$ matrix applied to truncate the **x** vector,

$$\mathbf{T} = \begin{bmatrix} 0 & 0 & 0 & 0 & 1 & 0 & \cdots & \cdots & 0 \\ 0 & 0 & 0 & 0 & 0 & \ddots & \ddots & \ddots & \vdots \\ \vdots & \vdots & \vdots & \vdots & \vdots & \ddots & \ddots & \ddots & \vdots \\ \vdots & \vdots & \vdots & \vdots & \vdots & \ddots & \ddots & \ddots & 0 \\ 0 & 0 & 0 & 0 & 0 & \cdots & \cdots & 0 & 1 \end{bmatrix}. \tag{7}$$

Then, the result of the combination approach is given as

$$\mathbf{x}_c = \left(\mathbf{T}^T\mathbf{C}^{-1}\mathbf{T} + \mathbf{SY}^T\mathbf{OC}_o^{-1}\mathbf{OYS}\right)^{-1}\left(\mathbf{T}^T\mathbf{C}^{-1}\mathbf{x}_g + \mathbf{SY}^T\mathbf{OC}_o^{-1}\mathbf{h}\right), \tag{8}$$

where $\mathbf{x}_c$ ($L \times 1$) denotes the set of re-estimated SHCs obtained after combining the two data sets, with the first four elements being the degree-1 and C_{20} coefficients; **C** ($L_g \times L_g$) is the full noise variance-covariance matrix of the SHCs from GRACE and $\mathbf{C}_o$ ($K \times K$) is the noise variance-covariance matrix of the oceanic mass anomalies.

2.2 Input data in general terms

2.2.1 GRACE data and their noise covariance matrices

The input GRACE SHCs ($\mathbf{x}_g$) are the Stokes coefficients (named GSM product). Such coefficients are cleaned for tidal contributions (with the use of a particular ocean tide model). Non-tidal atmospheric and oceanic contributions are also removed from GRACE observations in the level-1 data processing using the Atmosphere and Ocean De-aliasing level-1B (AOD1B) products (Flechtner & Dobslaw 2013). Monthly averages of the removed non-tidal effects are provided in the form of SHCs in the so-called GAC files. GAD files are the same as GAC, but restricted to ocean areas. However,

the oceanic contributions are from an OBP model, which conserves the ocean water mass. Water exchange between ocean and land is thus ignored. Also, the OBP model does not take into account SAL effects. Consequently, the total ocean mass change signal as well as the fingerprints due to SAL effects remain in the GSM coefficients.

As for the noise covariance matrices of GRACE data, CSR RL05 solutions (truncated at degree 60) are used throughout the study.

2.2.2 Oceanic data and their noise covariance matrices

Oceanic mass anomalies are provided by an OBP model, which is also used to produce GRACE GSM coefficients. In order to be compatible with the input GRACE data, tidal and non-tidal oceanic contributions should be removed from the oceanic data. As a result, when working with GRACE GSM coefficients, oceanic mass anomalies predicted by the OBP model are set equal to zero. As mentioned, we need to additionally estimate the signals caused by ocean-land mass exchange and fingerprints. Here, we estimate the total ocean mass variations by integrating GRACE-derived mass anomalies over oceans. Then we account for SAL effects and determine the fingerprints in ocean waters (Mitrovica *et al.* 2001) by solving the sea level equation (Farrell & Clark 1976; Tamisiea *et al.* 2010). It is worth noting that using GRACE to estimate the total ocean mass variation requires a complete GRACE solution including degree-1 and C_{20} coefficients in the CF frame. Therefore, total ocean mass variation is determined through an iterative procedure. The four targeting coefficients are null as a starting point and later updated with estimates of these coefficients. The total ocean mass variation as well as the estimated coefficients converge quickly with only 3 or 4 iterations (thereafter, the difference between the subsequent solutions is smaller than 0.1 per cent, see also Fig. 1).

Unlike for GRACE data, the error covariances of the OBP estimates are not provided directly. In the following, we will estimate the uncertainty σ_k at each oceanic data point in order to construct, at least, a diagonal error variance for the OBP estimates.
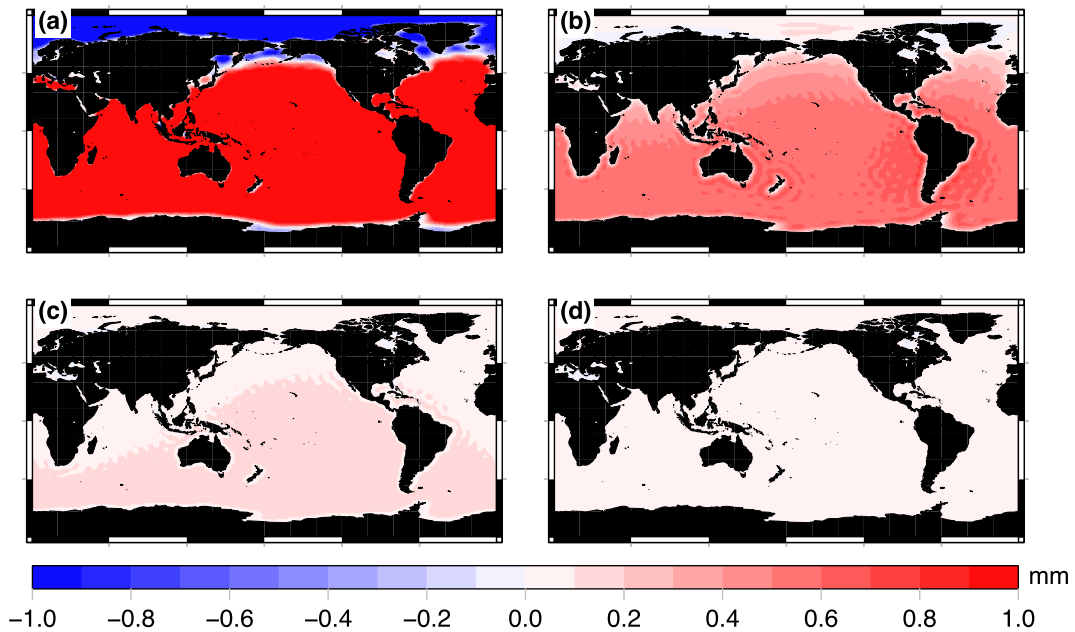

Figure 1. Oceanic mass anomalies updates at different iterations. In panels (a)–(d), we show the updates for iteration 1 (RMS: 2 mm; maximum value: 6 mm), iteration 2 (RMS: 0.4 mm; maximum value: 0.8 mm), iteration 3 (RMS: 0.08 mm, maximum value: 0.2 mm) and iteration 4 (RMS: 0.01 mm, maximum value: 0.03 mm), respectively.

Since the oceanic mass anomaly is a combination of the OBP model output (the OBP model error has to be considered even though the residual signal is zero) and the fingerprints, the RMS error σ_k at a given ocean point can be easily computed under the assumption that the error from these two sources are not cross-correlated:

$$\sigma_k^2 = \sigma_{obp,k}^2 + \sigma_{fts,k}^2, \tag{9}$$

where $\sigma_{obp,k}$ and $\sigma_{fts,k}$ are the RMS errors of OBP and fingerprints, respectively. The computation of them is described in Section 4.2.

The matrix $\mathbf{C}_o$ is defined as a diagonal matrix. Ignoring the error correlations may result in the overestimation of the OBP model accuracy and, therefore, in a too high weight assigned to the OBP predictions. In order to overcome this problem, we propose to scale the diagonal matrix $\mathbf{C}_o$ uniformly by a factor α.

$$\{\mathbf{C}_o\}_{(k,k)} = \alpha\sigma_k^2, \tag{10}$$

The optimal choice of alpha will be discussed later in Section 4.2. Therefore, we can introduce a diagonal weight matrix

$$\mathbf{P} = \mathbf{O}\mathbf{C}_o^{-1}, \tag{11}$$

with elements equal to

$$\{\mathbf{P}\}_{(k,k)} = \begin{cases} \frac{1}{\alpha\sigma_k^2} & \text{if } k \text{ is a point in ocean} \\ 0 & \text{if } k \text{ is a point on land.} \end{cases} \tag{12}$$

Finally, eq. (8) can be re-written as

$$\mathbf{x}_c = (\mathbf{T}^T\mathbf{C}^{-1}\mathbf{T} + \mathbf{S}\mathbf{Y}^T\mathbf{P}\mathbf{Y}\mathbf{S})^{-1}(\mathbf{T}^T\mathbf{C}^{-1}\mathbf{x}_g + \mathbf{S}\mathbf{Y}^T\mathbf{P}\mathbf{h}). \tag{13}$$

2.3 Relation with the GRACE-OBP method

The basic ideas behind the combination approach and the GRACE-OBP approach are very similar. Here, we show how the two methods are inter-related.

Let us define $\mathbf{x}_e$ as a 4×1 vector with entries equal to the degree-1 and C_{20} coefficients and $\mathbf{x}_g$ as a $(L-4) \times 1$ vector containing coefficients provided by GRACE (C_{20} coefficient is excluded). Assume that both $\mathbf{x}_e$ and $\mathbf{x}_g$ are free of errors. Then, the whole set of error-free SHCs $\mathbf{x}$ can be represented as:

$$\mathbf{x} = \mathbf{T}_e^T\mathbf{x}_e + \mathbf{T}^T\mathbf{x}_g, \tag{14}$$

where $\mathbf{T}_e$ is a $4 \times L$ matrix:

$$\mathbf{T}_e = \begin{bmatrix} 1 & 0 & 0 & 0 & 0 & \cdots & 0 \\ 0 & 1 & 0 & 0 & 0 & \cdots & 0 \\ 0 & 0 & 1 & 0 & 0 & \cdots & 0 \\ 0 & 0 & 0 & 1 & 0 & \cdots & 0 \end{bmatrix}. \tag{15}$$

The second line in eq. (6) can be written as

$$\mathbf{h} = \mathbf{O}\mathbf{Y}\mathbf{S}\left(\mathbf{T}_e^T\mathbf{x}_e + \mathbf{T}^T\mathbf{x}_g\right) = \mathbf{O}\mathbf{Y}\mathbf{S}\mathbf{T}_e^T\mathbf{x}_e + \mathbf{h}_g, \tag{16}$$

Thereby, $\mathbf{h}_g$ ($K \times 1$) represents oceanic mass anomalies without the contribution from the degree-1 and C_{20} coefficients. We subtract $\mathbf{h}_g$ from both sides of eq. (16), which allows us to isolate the contribution of the degree-1 and C_{20} coefficients. That is

$$\mathbf{h} - \mathbf{h}_g = \mathbf{O}\mathbf{Y}\mathbf{S}\mathbf{T}_e^T\mathbf{x}_e. \tag{17}$$

Note that $\mathbf{T}_e^T\mathbf{T}_e$ yields an idempotent matrix, that is, $\mathbf{T}_e^T\mathbf{T}_e = \mathbf{T}_e^T\mathbf{T}_e\mathbf{T}_e^T\mathbf{T}_e$; $\mathbf{S}$ and $\mathbf{T}_e^T\mathbf{T}_e$ commute because they are diagonal

matrices, that is, $\mathbf{S}\mathbf{T}_e^T\mathbf{T} = \mathbf{T}_e^T\mathbf{T}\mathbf{S}$. As a result, eq. (17) can be written as:

$$\begin{aligned} \mathbf{h} - \mathbf{h}_g &= \mathbf{O}\mathbf{Y}\mathbf{S}\mathbf{T}_e^T\mathbf{T}_e\mathbf{x} \\ &= \mathbf{O}\mathbf{Y}\mathbf{S}\mathbf{T}_e^T\mathbf{T}_e\mathbf{T}_e^T\mathbf{T}_e\mathbf{x} \\ &= \mathbf{O}\mathbf{Y}\mathbf{T}_e^T\mathbf{T}_e\mathbf{S}\mathbf{T}_e^T\mathbf{T}_e\mathbf{x} \\ &= \mathbf{O}\mathbf{Y}'\mathbf{S}'\mathbf{x}_e. \end{aligned} \tag{18}$$

where $\mathbf{Y}'$ is a $K \times 4$ matrix and $\mathbf{S}'$ is 4×4 matrix; they are the same as $\mathbf{Y}$ and $\mathbf{S}$, but only for the degree-1 and C_{20} coefficients. Eq. (18) can be considered as a linear functional model connecting an unknown vector $\mathbf{S}'\mathbf{x}_e$ and data vector $\mathbf{h} - \mathbf{h}_g$. Then, $\mathbf{x}_e$ can be solved for by plain linear regression. The obtained equation

$$\mathbf{S}'\mathbf{Y}'^T\mathbf{O}\mathbf{Y}'\mathbf{S}'\mathbf{x}_e = \mathbf{S}'\mathbf{Y}'^T\mathbf{O}\mathbf{h} - \mathbf{S}'\mathbf{Y}'^T\mathbf{O}\mathbf{h}_g, \tag{19}$$

or

$$\mathbf{Y}'^T\mathbf{O}\mathbf{Y}'\mathbf{S}'\mathbf{x}_e = \mathbf{Y}'^T\mathbf{O}\mathbf{h} - \mathbf{Y}'^T\mathbf{O}\mathbf{h}_g, \tag{20}$$

is the same as eq. (12) in Swenson *et al.* (2008) if written out explicitly (see Appendix B). The resulting solution is optimal provided that the noise in $\mathbf{h} - \mathbf{h}_g$ is white. Therefore, if the GRACE data are noise-free (so that $\mathbf{h}_g$ contains deterministic values and one does not have to estimate $\mathbf{x}_g$) and the noise in OBP data is white, the combination approach reduces to the GRACE-OBP approach.

3 IMPLEMENTATION PARAMETERS

In Sun *et al.* (2016a), we have already shown that estimates of degree-1 and C_{20} time-series based on the GRACE-OBP approach are controlled by at least three implementation parameters: (i) maximum degree of the input GSM coefficients, (ii) width of the buffer zone (a periphery surrounding the continents due to the application of a shrunk ocean function) and (iii) whether to consider SAL effects when distributing water over oceans or not. Sun *et al.* (2016b) addressed the optimal choice of implementation parameters by means of numerical simulations. They showed that the set of input GSM coefficients should be truncated between degrees 30 and 50, in order to include mass re-distribution at large spatial scales while excluding high-degree coefficients contaminated by large errors. The buffer zone should be around 200 km to mitigate the impact of continental signal leakage. Also, the ocean water has to be distributed realistically by taking into account SAL effects. We expect that the optimal truncation degree and the buffer zone width found in Sun *et al.* (2016b) will not change significantly in the combination approach. Therefore, we limit ourselves to the most promising combinations of implementation parameters. We test truncation degrees between 10 and 60, and buffer zones widths of 100, 200 and 300 km; SAL effects are always taken into account.

4 NUMERICAL EXPERIMENTS

Numerical experiments are carried out to verify the correctness and evaluate the performance of our methodology.

4.1 Simulation of GRACE GSM coefficients

The procedure to generate GRACE GSM coefficients is very similar to that described by Sun *et al.* (2016b). It is based on the updated ESA Earth System Model (ESM), which covers the period from 1995 to 2016 and is complete to spherical harmonic degree 180
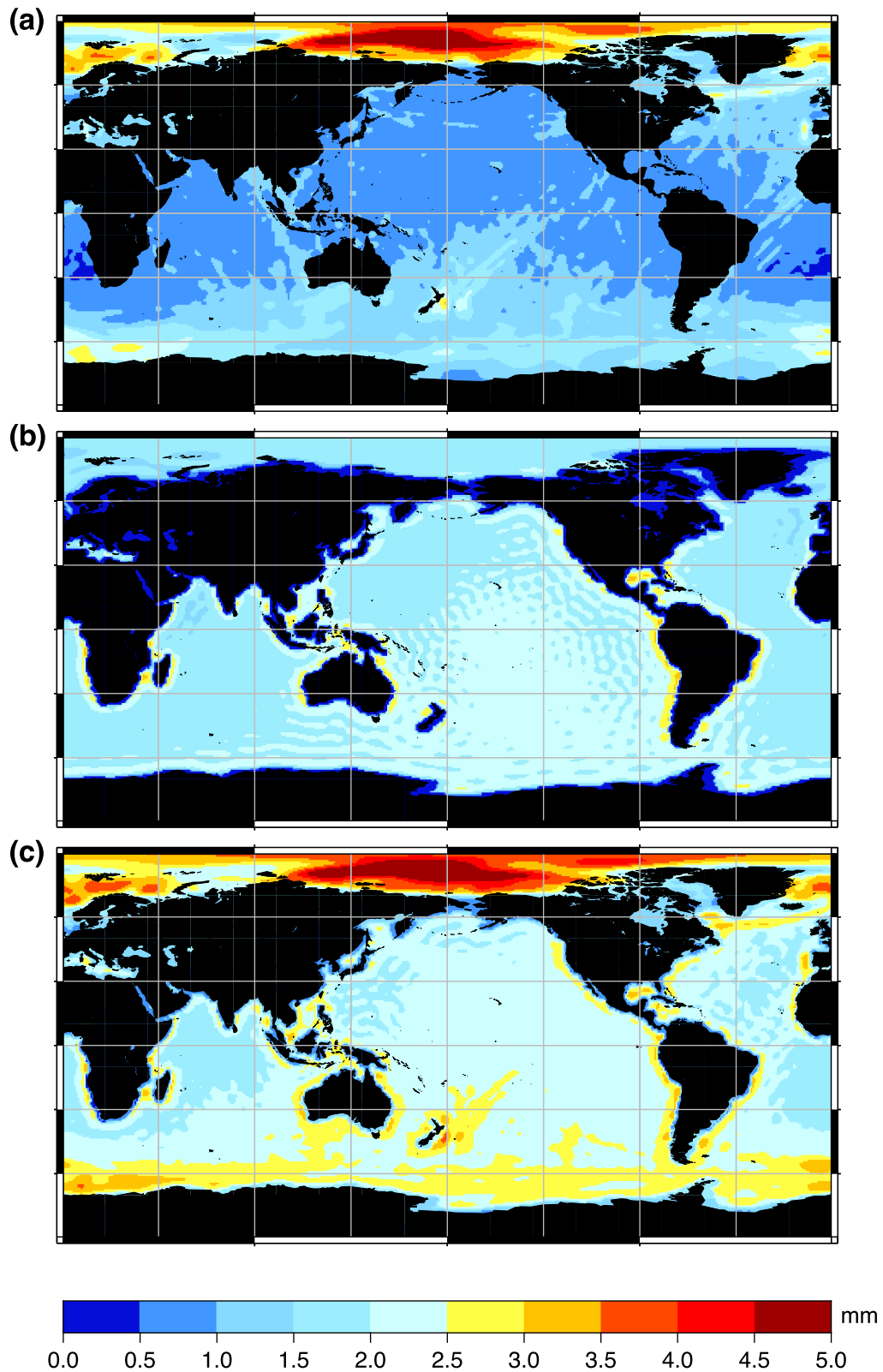
Figure 2. Uncertainty of oceanic mass anomalies. (a) The RMS error of OBP predictions. (b) The RMS error of fingerprints. (c) Total RMS error obtained with eq. (9).

(Dobslaw *et al.* 2015). It employs state-of-the-art geophysical models to simulate gravity changes due to mass re-distribution within the Earth system. It is worth noting that we have added SAL effects to the original ESM model. We sum up the contributions of the atmosphere, ocean, continental water, and ice-sheet components to mimic GRACE-sensed gravity changes due to surface mass redistribution. The error-free GSM coefficients are then generated by removing the monthly average of the dealiasing product, called DEAL coefficients, which represent a simplified model of mass transport in the atmosphere and ocean; they play the same role as the AOD1B product. The DEAL coefficients are provided together with the ESM. Two types of errors present in real GRACE GSM are added to the simulated error-free GSM coefficients to obtain realistically perturbed ones. First, random errors are simulated using the CSR RL05 monthly noise covariance matrices complete to degree 60. To make the results more representative, we generate ten error realizations per month. Second, we additionally introduce one realization of errors in the DEAL product, which is provided together with the ESM as the so-called AOerr files. The errors documented in the AOerr files are first defined as the differences between the updated ESM (the one used in this study) and the original ESM model, and then upscaled to match the uncertainty estimated by pairwise model comparisons based on a small ensemble (four) of atmospheric and oceanic models.

As a result, ten sets of noisy GSM coefficients per month are at our disposal. The sets are contaminated by different random errors and the same AOerr errors. For more details regarding the data simulation procedure, the reader is referred to (Sun *et al.* 2016b).

4.2 Determination of oceanic noise variances

The combination approach requires stochastic information about errors in the oceanic mass anomalies, which is not directly available. In this study, we estimate the RMS error σ_k at each data point of a 1×1 degree ocean grid. According to eq. (9), one needs to know the RMS error $\sigma_{obp,k}$ (for the OBP mass anomaly) and the RMS error $\sigma_{fts,k}$ (for the fingerprint mass anomaly). To obtain $\sigma_{obp,k}$, we use the OBP error estimates provided by the ESM. Since only one error realization per monthly OBP is given, we assume that the OBP noise is stationary in the time domain and calculate the RMS error per grid node using all monthly error estimates (Fig. 2a). For $\sigma_{fts,k}$, we calculate fingerprints from ten realizations of simulated noisy GSM coefficients. Assuming that the fingerprint noise is also stationary in the time domain, we compute the RMS error by averaging errors over months and noise realizations (Fig. 2b). Finally, σ_k (Fig. 2c) is computed through eq. (9).

As explained in Section 2.2.2, a scaling factor (α) has to be introduced to account for the lack of information about OBP error covariances. To estimate the scaling factor, we use two criteria. First, the scaled error covariance matrix $\mathbf{C}_o$ should result in minimal Actual RMS Errors (ARE) when comparing the resultant degree-1 and C_{20} estimates with the synthetic truth. Second, the obtained Formal RMS Errors (FRE) for degree-1 and C_{20} solutions should be of similar magnitude as the ARE. To make the calculation of ARE and FRE easier to understand, we visualize them in Fig. 3.

We calculate the ARE ($e_{ARE}^{cf,n}$) and the FRE ($e_{FRE}^{cf,n}$) for a particular coefficient (indicated by superscript *cf*, which runs over the four estimated mass SHCs, namely C_{10}, C_{11}, S_{11} and C_{20}) based on the *n*th GSM realization. The best scaling factor, however, is different from coefficient to coefficient and from realization to realization. To obtain a uniform choice, we further calculate the combined ARE
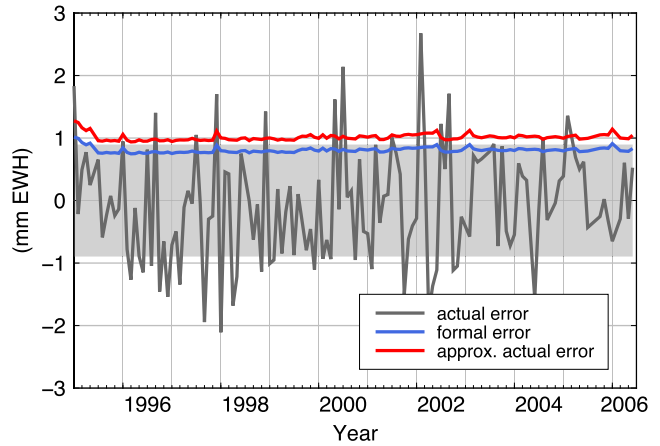

Figure 3. Actual error, actual RMS error (ARE) and approximated actual RMS error (approx. ARE) for one realization of synthetic C_{10} coefficients. The actual errors are obtained as the differences between the resulting C_{10} time-series and the synthetic truth. ARE is then obtained as the RMS difference, which is shown as a grey band (the upper and lower bound of the grey band is then $\pm$ ARE).
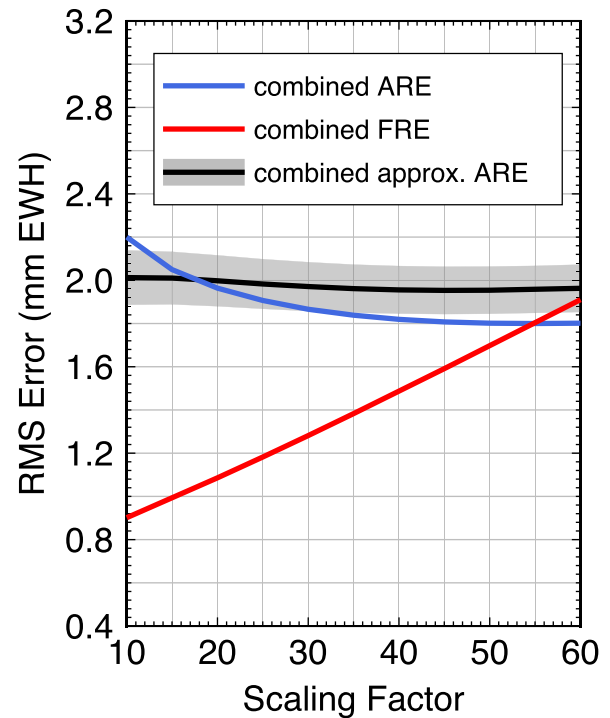

Figure 4. Combined ARE, combined FRE and combined approximated ARE as functions of the scaling factor. The grey band along the combined approximated ARE curve shows its STD from 10 GSM realizations. Note that the parameter setup is as follows: truncation degree: 50, buffer zone width: 200 km.

(e_{ARE}^{cmb}) and the combined FRE (e_{FRE}^{cmb}) (shown in Fig. 4 as a function of scaling factor):

$$e_{ARE}^{cmb} = \sqrt{\sum_{cf=C_{10}}^{C_{20}} \left(\text{AVR} \left\langle e_{ARE}^{cf,n}, (n = 1, 2, \ldots, N) \right\rangle \right)^2},$$

$$e_{FRE}^{cmb} = \sqrt{\sum_{cf=C_{10}}^{C_{20}} \left(\text{AVR} \left\langle e_{FRE}^{cf,n}, (n = 1, 2, \ldots, N) \right\rangle \right)^2}, \quad (21)$$
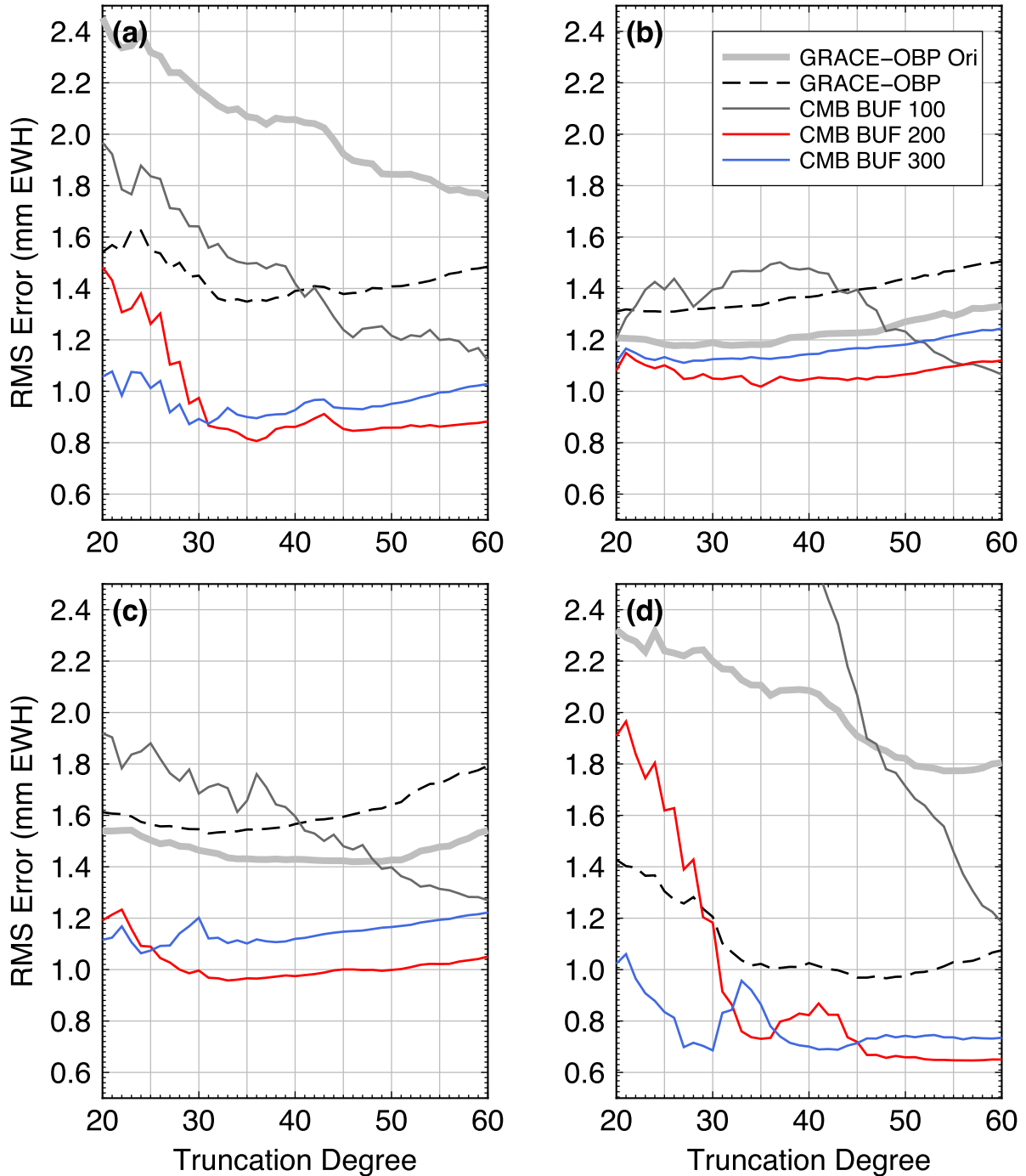
Figure 5. The RMS errors (average over 10 simulated GSM solutions) for resulting degree-1 and C_{20} coefficient time-series (in mm of equivalent water height). Results for C_{10}, C_{11}, S_{11} and C_{20} are presented in panels (a)–(d), respectively. The thick grey lines show the results of the GRACE-OBP-Swenson approach. The dashed grey lines indicate solutions based on the GRACE-OBP-Improved approach considering SAL effects and using a 200 km buffer zone.

where N is the number of sets of simulated GSM coefficients ($N = 10$). Further increasing N does not change the results significantly. AVR ⟨ ⟩ is the operator of averaging RMS errors over all error realizations. Note that according to the Parseval's identity, the sum of squared spherical harmonic coefficients describing the mass transport function is equal (up to a constant scaling factor) to the squared L2-norm of the mass transport function itself.

As α increases, the combined ARE decreases until convergence (within 1 per cent for $\alpha > 45$), whereas the combined FRE increases linearly. The decrease of the combined ARE means that the obtained

solution gets closer to the statistically optimal one, which is an indication that the assumed errors in the OBP estimates become more reasonable as α increases. A proper choice for the scaling factor is therefore at the intersection of the two curves, which is around 55 (corresponds to the upscaling of the RMS error with a factor of about 7.5). It is worth noting that the optimal scaling factor does not change significantly with different implementation parameter setups (not shown). Such a large value of α might seem odd for a synthetic experiment, but it is justified by the fact that the OBP model used here is not provided with an error covariance

matrix. The noise added to the error-free OBP estimates is not generated from a provided error covariance matrix but taken from an existing noise realization provided by Dobslaw *et al.* (2016). Based on this noise realization, we construct the diagonal error covariance matrix for the OBP data. A large α is expected to account for the discrepancy between the actual stochastic properties of exploited noise realization (which is correlated in the spatial domain) and the adopted noise covariance matrix, which is diagonal (and, therefore, does not take noise correlations into account).

In real data processing, information of ARE is not available. Therefore, we propose to estimate the actual error using the approach of Ditmar *et al.* (2017), which allows us to approximate the actual error in a time-series without the knowledge of the true signal (More information can be found in Appendix C).

The conducted numerical study allows us to validate that procedure in the context of low-degree coefficients. In Fig. 3, we also show an example of time-series of the estimated RMS of the actual errors. We calculate the combined approximated ARE for the four coefficients ($e^{\text{cmb}}_{\text{approx. ARE}}$) following a similar equation as eq. (21):

$$e^{\text{cmb}}_{\text{approx. ARE}} = \sqrt{\sum_{cf=C_{10}}^{C_{20}} \left(\text{AVR} \left\langle e^{cf,n}_{\text{approx. ARE}}, (n = 1, 2, \ldots, N) \right\rangle \right)^2}.$$

(22)

Clearly, $e^{\text{cmb}}_{\text{approx. ARE}}$ is the average over ten error realizations. This is not the case when dealing with real data, where only one error realization (true error) present. Fortunately, the $e^{cf,n}_{\text{approx. Err}}$ does not change significantly from realization to realization (see the grey band in Fig. 4).

For all error realizations, the scaling factor determined from the approximated actual error and the formal error is fairly close to the optimal scaling factor, which is equal to 55 in the considered case. Therefore, it is recommended to use the same procedure when processing real data. The obtained formal error will change linearly if the scaling factor determined differs from the optimal one.

4.3 Quality indicator

The resulting degree-1 and C_{20} time-series based on each parameter combination are compared with the synthetic truth (the scaling factor α is fixed to 55). Our goal is to select the setup that leads to the minimal RMS error of the resulting time-series. To that end, we compute the RMS of the differences between the resulting time-series ($T(C_{lm}^{(h)})$) and the synthetic truth ($T(C_{lm}^{t(h)})$) in terms of equivalent water heights. In Fig. 5, we show the RMS errors for all the tested parameter combinations (as functions of the truncation degree). Best estimates for degree-1 and C_{20} time-series are obtained with a 200-km buffer zone and a truncation degree between 30 and 50. For C_{20}, it becomes worse around degree 40 for reasons that are still under investigation. We also show the RMS errors for solutions based on the GRACE-OBP-Improved method (200-km buffer width, SAL effects are taken into account) for comparison. Additionally, we show the results obtained with the original implementation parameters of Swenson *et al.* (2008). The combination approach clearly outperforms the two latter approaches by producing solutions with lower RMS errors.

However, our goal is to determine the unified optimal parameter setup that would lead to the best estimation of all the considered coefficients. To this end, we use the sum of error variances of the
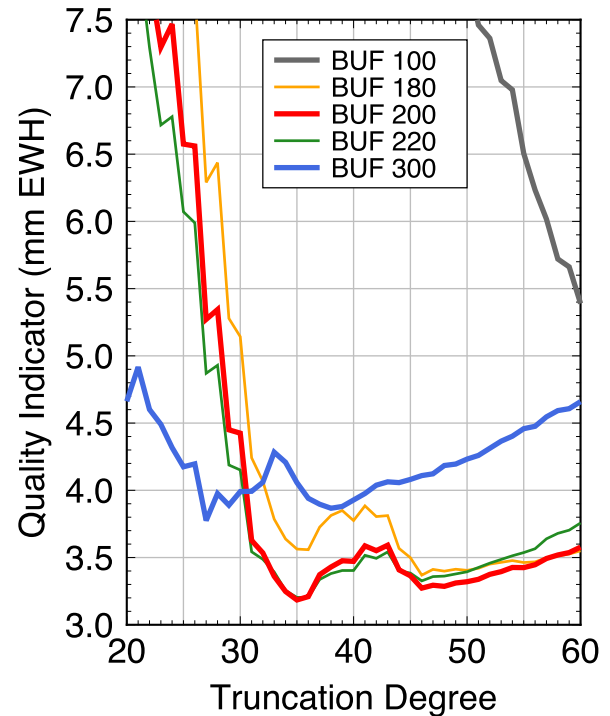

Figure 6. The same as Fig. 5, but the unified quality indicator is shown instead of RMS errors per coefficient.

four coefficient time-series as the overall quality indicator (QI):

$$\text{QI} = \frac{1}{N} \sum_{n=1}^{N} \left(\text{VAR} \left\langle T\left(C_{10}^{(h)}\right)^n - T\left(C_{10}^{t(h)}\right) \right\rangle \right.$$
$$+ \text{VAR} \left\langle T\left(C_{11}^{(h)}\right)^n - T\left(C_{11}^{t(h)}\right) \right\rangle$$
$$+ \text{VAR} \left\langle T\left(S_{11}^{(h)}\right)^n - T\left(S_{11}^{t(h)}\right) \right\rangle$$
$$\left. + \text{VAR} \left\langle T\left(C_{20}^{(h)}\right)^n - T\left(C_{20}^{t(h)}\right) \right\rangle \right),$$

(23)

where VAR $\langle \rangle$ is the operator for calculating the variance of a time-series; n indicates the data set number ($n = 1, 2, \ldots, N$), and N is the total number of data sets ($N = 10$). Note that all the coefficients are defined in terms of equivalent water height. Our intention is to choose the parameter setting that leads to the lowest QI value. Fig. 6 shows that a truncation degree larger than 35 and a buffer width of 200 km are the preferred setup.

While the QI values give an indication of the overall quality of the resultant degree-1 time-series, it is the annual cycle (the largest periodic signal) that is particularly interesting. In Figs 7 and 8, we show the mean annual amplitude and phase estimates of degree-1 and C_{20} time-series and their standard deviations (indicated by light coloured bands). For annual amplitudes (Fig. 7), the estimates are getting closer to the synthetic truth as the truncation degree increases. However, when using the narrow buffer (100 km), one cannot recover the true annual amplitude with any truncation degree for C_{10}, S_{11} and C_{20}. With a wider buffer (200 or 300 km), we can recover the annual amplitude within 10 per cent for all four coefficients when using truncation degrees higher than 35. For annual phase estimates, we see less dependence on the implementation parameters. In most cases (except for the C_{10} estimates based on a 100 km buffer zone) one can recover the true annual phase within 5 d. In addition to the QI mentioned above, we compute the QI for annual variations based on Sun *et al.* (2016b) (eq. 7). Consideration of
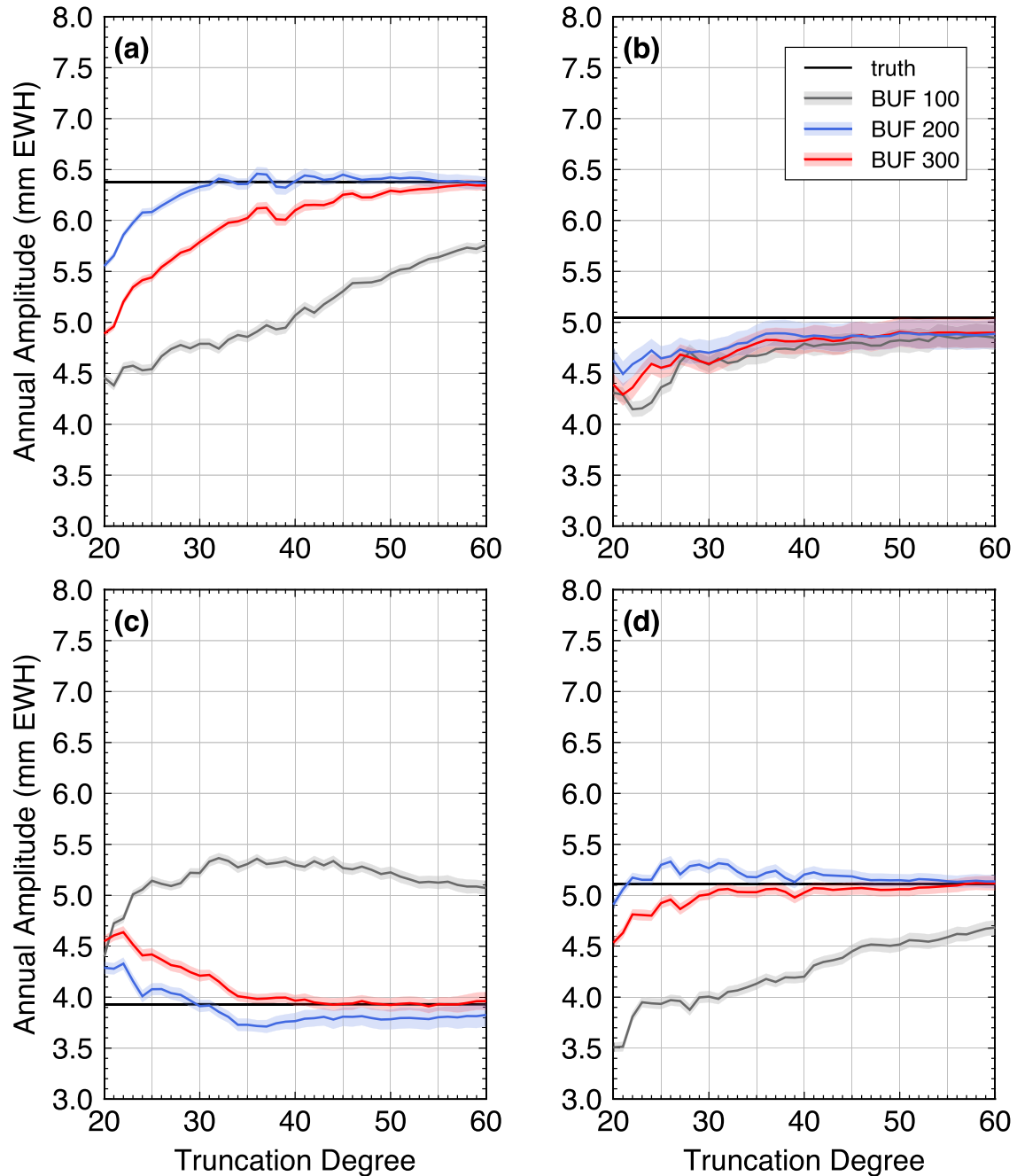
Figure 7. The mean annual amplitudes of the GSM degree-1 and C_{20} time-series (mm EWH) estimated using different implementation parameters, based on 10 sets of simulated GSM solutions. The standard deviations of amplitude estimates (based on 10 sets of GSM solutions) are indicated by light coloured bands. The true amplitudes are marked in all panels as black horizontal lines. Results for C_{10}, C_{11}, S_{11} and C_{20} are shown in panels (a)–(d), respectively.

this criterion confirms that, larger truncation degrees are beneficial for estimating annual variations (Fig. 9).

Ultimately, we recommend to use a truncation degree of 50 and buffer width of 200 km. In Sun *et al.* (2016b), the same buffer width was selected but the truncation degree was 45.

The selected parameter setup ensures good estimates of both overall quality and annual variations in all four coefficients.

5 RESULTS BASED ON REAL DATA

We produce degree-1 and C_{20} time-series using real GRACE data as input. The CSR RL05 GRACE monthly solutions (complete

to degree 60) for a 12 yr period from August 2002 to June 2014 and their corresponding noise variance-covariance matrices are used. We correct the input GSM coefficients for the pole tide according to Wahr *et al.* (2015). The GIA effects are corrected for by removing the GIA model computed by A *et al.* (2012) (degree-1 coefficients in the CF reference frame are kindly provided by the authors through personal communication. These modelled degree-1 trends are not used during the calculation, but can be useful at the last stage to restore the GIA contributions to the resulting degree-1 solutions). Other time-variable solid Earth signals are ignored as in previous studies (Swenson *et al.* 2008).
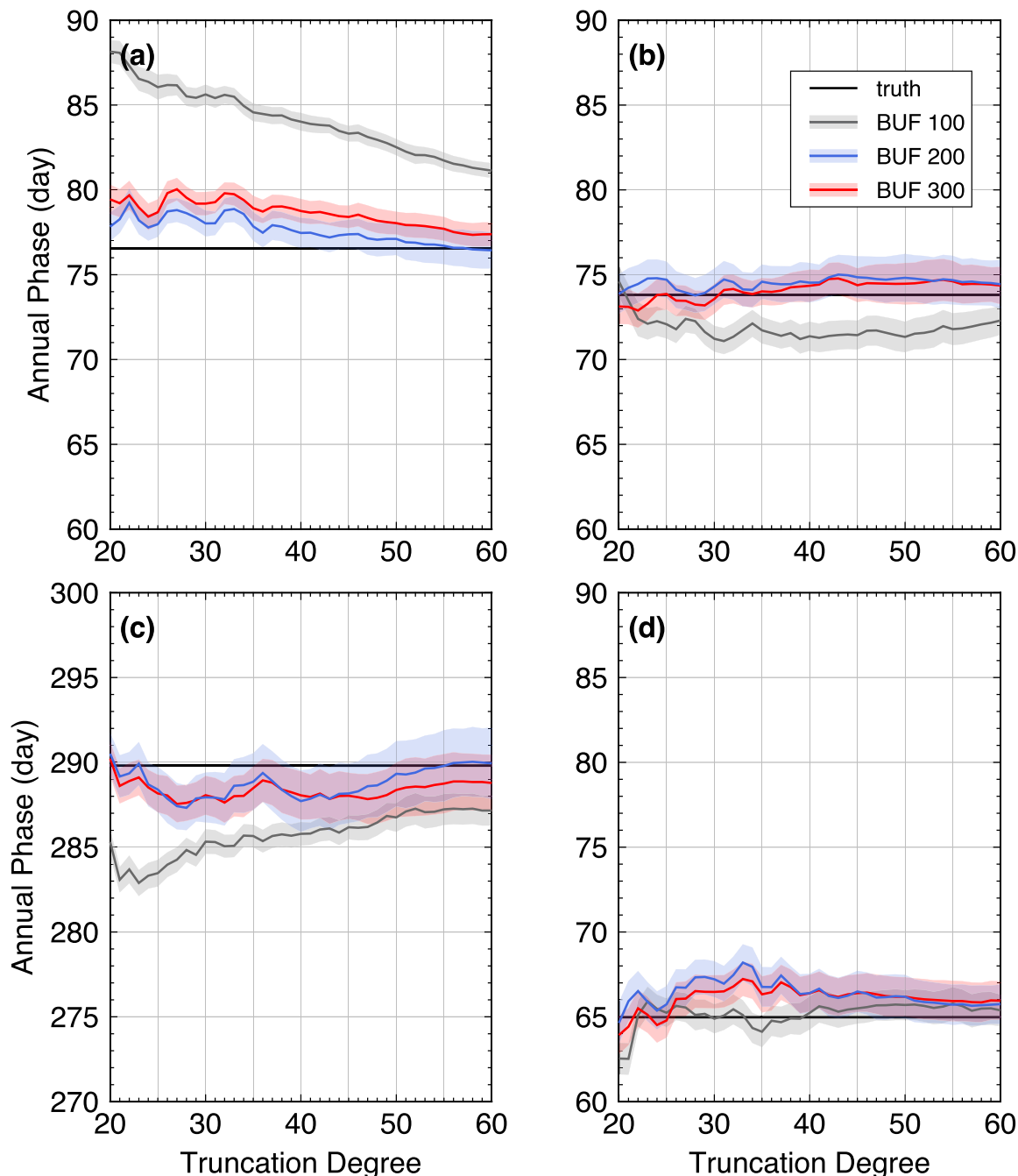
Figure 8. The same as Fig. 7, but for the annual phases.

The noise covariance matrix of the oceanic data is the same as determined in the numerical experiments, but scaled with a different scaling factor. In order to determine the proper scaling factor, a number of candidates (in the range from 50 to 150) are tested. For each scaling factor, we estimated the time-series of the four low-degree coefficients and the associated combined formal error. According to Fig. 10, the optimal scaling factor is 120. The choice of the scaling factor has minor effects on the estimated coefficients but strongly affects the formal error estimation.

The final time-series are shown in Fig. 11(a), where the degree-1 time-series are compared against the solutions from the GRACE-OBP-Swenson approach (Swenson *et al.* 2008), and the C_{20} time-series is compared to an SLR solution (Cheng *et al.* 2013a). Our C_{10} and C_{11} time-series have larger annual amplitudes while the S_{11}

time-series is almost indistinguishable from the Swenson's solution. Our C_{20} time-series is free of large anomalies with a period of 161 days and has other considerable differences from the SLR one, especially after 2011. Note that our C_{20} time-series shows a more pronounces annual cycle, which is reasonable in view of a seasonal mass exchange between oceans and continents.

We compare also the low-degree coefficients estimated with different techniques in terms of annual variations (Table 1), we see that annual variations predicted with the combination approach and the GRACE-OBP-Improved approach are in line with those based on independent techniques. An exception is a discrepancy in the annual phase estimates of C_{10}. Solutions based on GRACE and OBP data, including those based on the combination approach, the GRACE-OBP-Improved approach, and the GRACE-OBP approach, are more
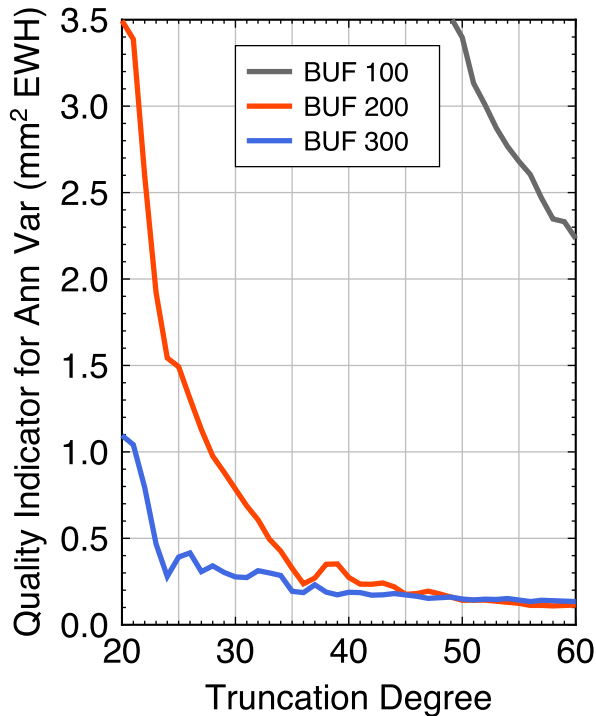
Figure 9. The same as Fig. 6, but the quality indicator for annual variations is shown instead of quality indicator for RMS error.
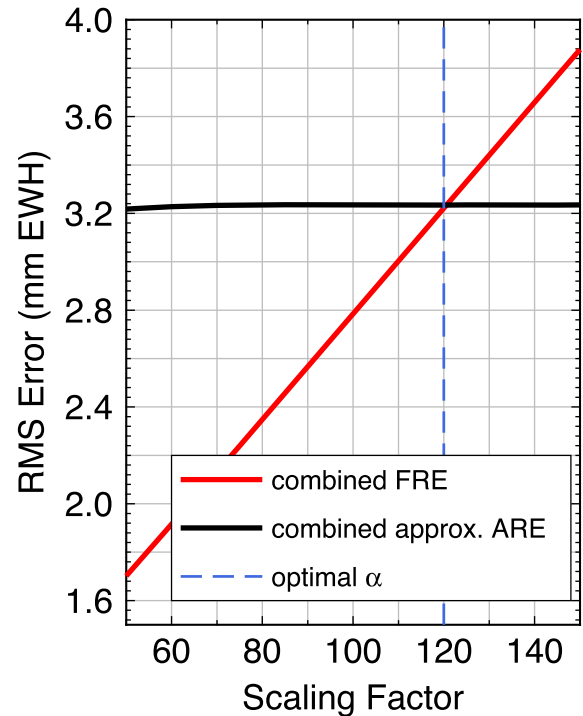

Figure 10. Combined FRE and combined approximated ARE as functions of the scaling factor. Note that the parameter setup is as follows: truncation degree: 50, buffer zone width: 200 km.

than a month behind those based on other techniques. We show in the next section (Section 6) that the GRACE-OBP-based solutions are likely more accurate.

One of the advantages of the combination approach is that it provides the noise variances and covariances of the estimated coefficients in a natural way (Fig. 11b). We show that the formal errors of degree-1 and C_{20} coefficients are different from month to month and generally larger than those documented in the product based on GRACE-OBP-Swenson (ftp://podaac.jpl.nasa.gov/allData/tellus/L2/degree_1/deg1_coef.txt). The correlations between the errors in these coefficients are rather small except those between C_{10} and C_{20} (Fig. 11c). This is expected because the polar areas play the major role in the separation of these coefficients (the corresponding surface spherical harmonics reach their local maxima in absolute value). However, there is a lack of oceanic data in the southern polar region caused by the presence of the Antarctica. On the other hand, the zonal degree-1 and -2 spherical harmonics in the northern polar region are of the same sign. This means that a positive error in the C_{10} coefficient can be largely compensated by a negative error in the C_{20} coefficient and vice versa. Thus, these errors must show a strong anti-correlation.

6 WHICH DEGREE-1 AND C_{20} SOLUTION TO USE FOR ESTIMATING MASS VARIATIONS?

Independent estimates of degree-1 and C_{20} coefficients are typically used to correct GRACE solutions in order to obtain more accurate estimates of surface mass anomalies. However, owing to the lack of an accurate reference regionally or globally, it is difficult to quantify the added value of this correction. GRACE users often adopt a specific solution without justification for their choice. In this section, we offer a simple way to evaluate the quality of degree-1 and C_{20} coefficients. GRACE GSM solutions are used to estimate mass

variations within particular regions where the mass variations are known to be minor, namely East Antarctica and the Sahara Desert (e.g. Helsen *et al.* 2008; Liu *et al.* 2010). These regions are used as validation areas. We estimate mass anomaly time-series there, using the GRACE solutions corrected with different variants of degree-1 and C_{20} time-series. The best degree-1 and C_{20} time-series should result in the smallest mass variations over the selected validation areas. Note that the mass anomalies over validation areas at different geographic locations may not be sensitive to all the coefficients. It is thus important to select more than one well-separated regions as the validation areas.

We have prepared 7 versions of GRACE solutions by using different combinations of degree-1 and C_{20} coefficients:

(i) **Ori GRC**: Original GRACE CSR RL05 solutions as they are. That is, zero degree-1 coefficients and the native GRACE C_{20} are adopted.

(ii) **SLRDeg1 + SLRC20**: GRACE solutions complemented with SLR-based degree-1 (Cheng *et al.* 2013b) and C_{20} coefficients (Cheng *et al.* 2013a).

(iii) **INVDeg1 + SLRC20**: GRACE solutions corrected with degree-1 coefficients based on the joint inversion approach (Rietbroek *et al.* 2016) (https://doi.pangaea.de/10.1594/PANGAEA.855539) and SLR C_{20} coefficients.

(iv) **SWEDeg1 + SLRC20**: GRACE solutions complemented with degree-1 coefficients based on the GRACE-OBP-Swenson approach (Swenson *et al.* 2008); C_{20} coefficients are based on SLR data . This is the traditionally used approach.

(v) **CMBDeg1 + CMBC20**: GRACE solutions corrected with the degree-1 and C_{20} coefficients provided by the combination approach.

(vi) **CMBDeg1 + SLRC20**: GRACE solutions corrected with the degree-1 coefficients provided by the combination approach and SLR C_{20} coefficients.
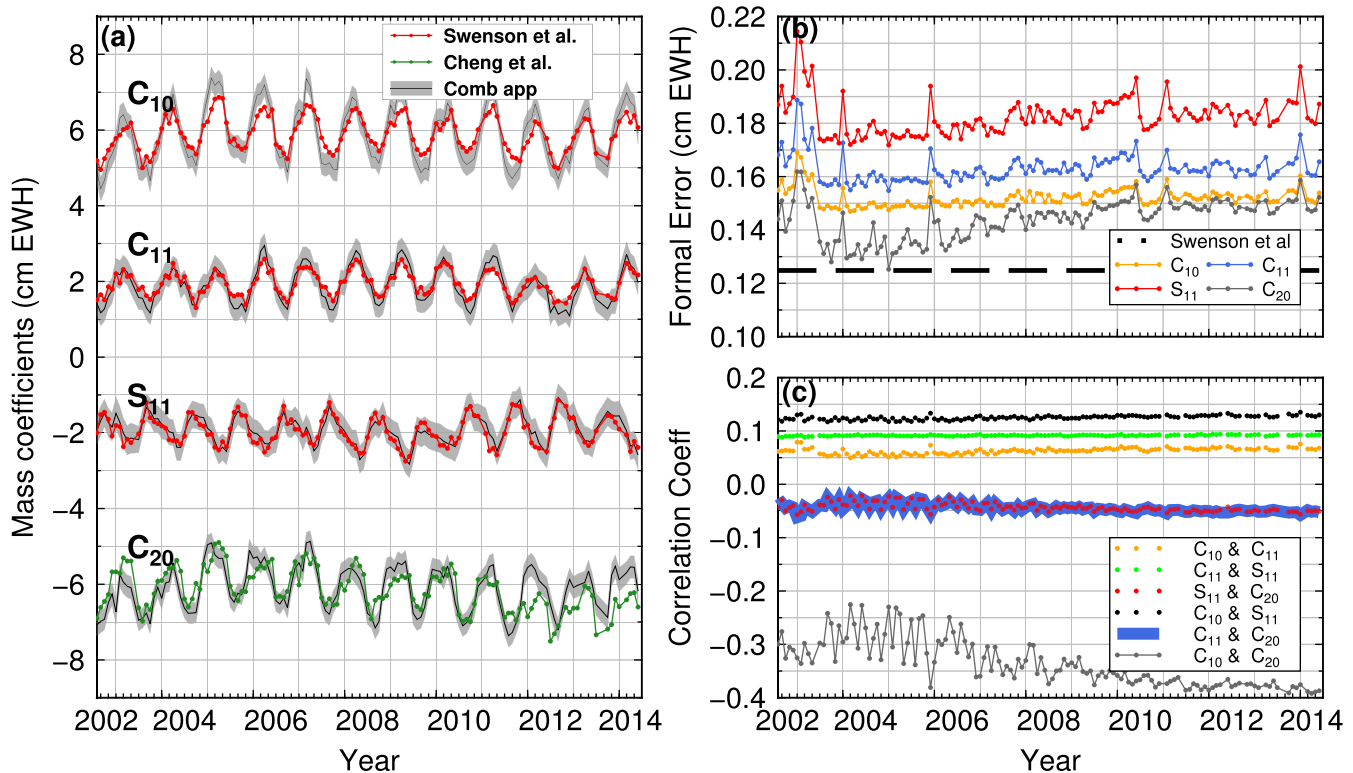
Figure 11. Final solutions for degree-1 and C_{20} time-series (a), their formal error estimates (b) and correlation coefficients (c) based on the combination approach. In panel (a), linear trends are removed. Results are offset for clarity. The coloured bands show the 2-σ uncertainties. The black dashed line shown in panel (b) (denoted as 'Swenson *et al.*') is taken from the official product based on (Swenson *et al.* 2008) (see the text).

Table 1. Estimated amplitudes and phases of the annual variations of degree-1 and C_{20} coefficients, based on real data. The contribution of atmosphere and ocean (GAC) is restored. Please note that the annual amplitude A and phase ϕ are defined by $A\cos(2\pi(t-t_0)-\phi)$, where t_0 refers to January 1 of a particular year. The solutions 'Combination approach *' and 'Combination approach **' are estimated over reduced time intervals to be more comparable with those from Wu *et al.* (2015) and Rietbroek *et al.* (2012).

| | C_{10} | | C_{11} | | S_{11} | | C_{20} | | |
	Amp (mm)	Pha (day)	Amp (mm)	Pha (day)	Amp (mm)	Pha (day)	Amp (10^{-11})	Pha (10^{-11})	Time span
Combination approach	3.2 ± 0.2	66 ± 3	2.4 ± 0.1	61 ± 3	2.6 ± 0.1	333 ± 2	16.2 ± 0.7	48 ± 3	2002 Aug – 2014 Jun
Combination approach *	3.1 ± 0.2	64 ± 3	2.4 ± 0.1	58 ± 3	2.6 ± 0.1	333 ± 2	15.7 ± 0.7	47 ± 3	2002 Aug – 2009 Apr
Combination approach **	3.0 ± 0.2	64 ± 3	2.5 ± 0.1	57 ± 3	2.6 ± 0.1	334 ± 2	15.4 ± 0.7	46 ± 3	2003 Jan – 2008 Dec
GRACE-OBP-Improved	2.9 ± 0.2	68 ± 3	2.3 ± 0.1	52 ± 3	2.9 ± 0.1	327 ± 2	16.1 ± 0.7	47 ± 3	2002 Aug – 2014 Jun
GRACE-OBP-Swenson	1.9 ± 0.1	65 ± 4	1.9 ± 0.1	53 ± 3	2.5 ± 0.1	319 ± 2			2002 Aug – 2014 Jun
INV (Rietbroek *et al.* 2012) 1	3.0	18	2.1	56	3.4	327			2003 Jan – 2008 Dec
INV (Rietbroek *et al.* 2012) 2	2.2	31	2.0	63	3.4	326			2003 Jan – 2008 Dec
INV (Rietbroek *et al.* 2016)	3.5 ± 0.1	66 ± 3	2.2 ± 0.1	58 ± 2	2.7 ± 0.1	325 ± 2			2002 Aug – 2014 Jun
(Wu *et al.* 2015) 1	3.9 ± 0.1	21 ± 1	2.1 ± 0.1	45 ± 1	2.7 ± 0.1	321 ± 1			2002 Apr – 2009 Apr
(Wu *et al.* 2015) 2	3.3 ± 0.1	22 ± 3	1.9 ± 0.1	54 ± 2	2.6 ± 0.1	322 ± 1			2002 Apr – 2009 Apr
(Wu *et al.* 2015) 3	3.5 ± 0.1	19 ± 1	1.9 ± 0.1	52 ± 1	3.0 ± 0.1	337 ± 1			2002 Apr – 2009 Apr
SLR (Cheng *et al.* 2013b)	4.2 ± 0.3	33 ± 2	2.9 ± 0.4	49 ± 4	2.7 ± 0.1	339 ± 2			2002 Aug – 2014 Jun
SLR (Cheng *et al.* 2013a)							14.1 ± 0.7	53 ± 3	2002 Aug – 2014 Jun

(vii) **GODeg1 + GOC20**: GRACE solutions corrected with the degree-1 coefficients and C_{20} provided by the GRACE-OBP-Improved approach (Sun *et al.* 2016b).

It should be noted that we have also used a filtered GRACE solution based on DDK-4 (Kusche *et al.* 2009). Besides, multiple sub-regions are selected as validation areas in each of two places. However, the results are very similar and thus we show the results based on one of the areas. The linear trends in the resultant mass transport time-series are subject to large uncertainties and are not

comparable. The linear trends in SLR-based degree-1 coefficients reflect merely drifting errors with respect to the origin of the International Terrestrial Reference Frame (ITRF). Degree-1 solutions from other considered approaches involve the use of a GIA model. However, the adopted GIA models are different and all contain large uncertainties of unknown magnitude. Therefore, trends and seasonal variations in the resulting mass transport time-series must be assessed independently. Here, we will focus on the seasonal variations (Sections 6.1 and 6.2). The quality of the trend estimates in our degree-1 and C_{20} solutions are not assessed in the following
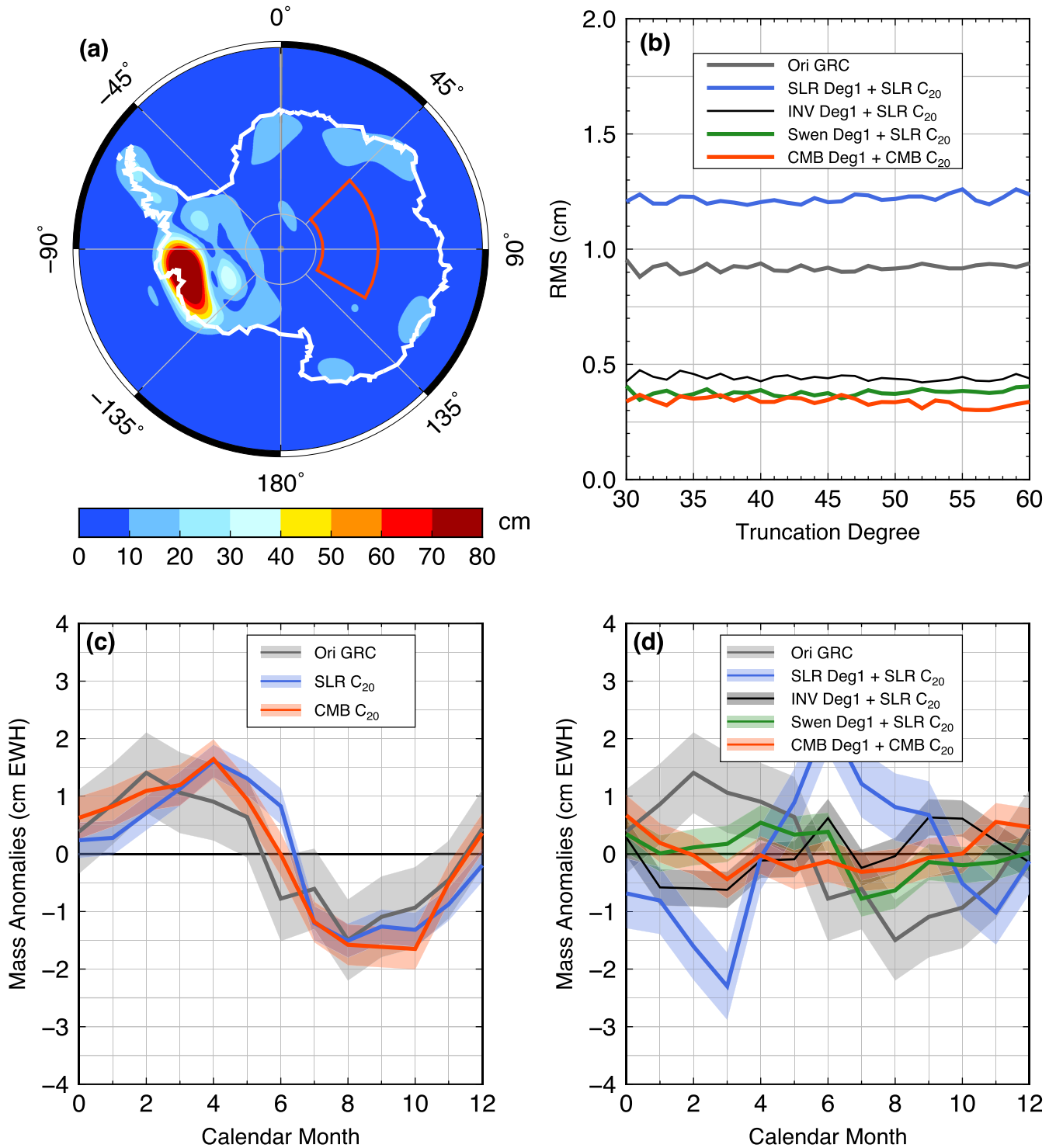
Figure 12. Mass variations in the validation area at East Antarctica. In panel (a), we show the signal RMS in terms of equivalent water heights. The study area is indicated with a red polygon (45°E/120°E/76°S/84°S). Panel (b) shows RMS values of mass anomaly time-series as a function of truncation degree. Panels (c) and (d) show the mean mass anomaly per calendar month. The shadowed colour bands indicates the spread of the monthly mass anomalies. Note that the calendar month 0 represents December of the previous year. In panel (c), we show the results based on the GRACE solutions after replacing the C_{20} coefficients with those from independent approaches. In panel (d), we show results when the GRACE solutions are further complemented with degree-1 coefficients based on different approaches.

experiments. Nevertheless, we show the resulting trend estimates in the mass transport time-series over both validation areas (Section 6.3). These trend estimates are obtained based on the assumption that the GIA model provided by A *et al.* (2012) is free of error. It is worth noting that under such an assumption, the combination approach, which is a generalised GRACE-OBP-Improved approach, should be able to recover the true linear trends in the degree-1 and C_{20} time-series (Sun *et al.* 2016b).

Table 2. RMS of mass anomaly (integrated over validation areas) obtained by averaging the corresponding time-series. In this table, we intend to show explicitly the numbers based on four solutions, namely, **Ori GRC**, **CMBDeg + CMBC20**, **CMBDeg1 + SLRC20** and **GODeg1 + GOC20** for a truncation degree of 50. See Section 6 for the meaning of abbreviations in the first column.

GRACE solutions	East Antarctic (cm)	Sahara Desert (cm)
Ori GRC	0.92	0.78
CMBDeg1 + CMBC20	0.33	0.35
CMBDeg1 + SLRC20	0.34	0.39
GODeg1 + GOC20	0.29	0.31

6.1 Mass variations in East Antarctica

There are no physical processes that would be able to cause large mass variations in the interior of East Antarctica (Helsen *et al.* 2008). Therefore, the GRACE solution augmented with the optimal degree-1 and C_{20} estimates should result in the minimal mass variations. However, one should bear in mind that mass anomalies in this region are sensitive to only the zonal coefficients, that is, C_{10} and C_{20}.

In the background of Fig. 12(a), we show the RMS mass anomaly based on the solution from the combination approach in the considered time interval (2002 - 2014). One of the tested regions (or validation areas) in this area is indicated in the panel with a red polygon. All variants of GRACE solutions are employed to estimate the total mass variations within the validation area, and the resulting RMS estimates of the de-trended mass variation time-series (as a function of the truncation degree) are shown in Fig. 12(b).

It can be seen that the RMS value of the mass variation time-series based on the original GRACE solution (**Ori GRC**) is about 0.9 cm. It reduces by more than 50 per cent when we use **INVDeg1 + SLRC20**, and is further reduced if we apply the **SWEDeg1 + SLRC20** or **CMBDeg1 + CMBC20**. Results based on the later solution is improved by about (10 20 per cent) compared to that based on the traditional approach. In contrast, using **SLRDeg1 + SLRC20** worsen the results by about 20 per cent. For clarity, results based on **CMBDeg1 + SLRC20** as well as **GODeg1 + GOC20** are not shown in the figure as they are very close to the **CMBDeg1 + CMBC20**, but the corresponding resultant RMS values of the time-series is documented in Table 2. We will discuss the results later in Section 7.

Note that the truncation degree of the GRACE solution (between 30 and 60) obviously plays a minor role in the RMS estimates, which implies that the validation area is large enough to ensure a cancellation of random errors in high-degree coefficients.

Subsequently, we calculate the mean mass anomaly per calendar month and show the effect of replacing C_{20} and adding degree-1 coefficients in panels (c) and (d), respectively. In the **Ori GRC** case, a clear seasonal pattern is revealed. Replacing the original C_{20} coefficients with those from SLR data and the combination approach show some differences but does not significantly change the resultant seasonal pattern (Fig. 12c). Such a seasonal pattern can thus be attributed to either the absence of the degree-1 coefficients or errors in higher-degree coefficients. However, the total mass variations of the validation area are obtained by integrating all data points within the area. Mass anomalies due to high-degree errors are random and would unlikely show a seasonal pattern. Also, as previously showed (Fig. 12b), increasing the truncation degree does not significantly change the RMS estimates of the mass transport time-series. This is an indication that the errors in high-degree coefficients indeed

largely cancel each other. Furthermore, different validation areas in East Antarctica are employed, but the revealed seasonal pattern is quite consistent. This contradicts to the nature of high-degree errors as their impact changes quickly from location to location. Therefore, we believe that the observed season pattern is mostly due to the lack of the degree-1 coefficients. Indeed, once the GRACE solutions are complemented with proper estimates of degree-1 coefficients (based on the joint inversion approach, GRACE-OBP-Swenson approach, or the combination approach), the seasonal pattern significantly reduces or disappears (Fig. 12d). Remarkably, after using degree-1 solutions from SLR, the resulting seasonal pattern is in anti-phase, as compared to the one produced without degree-1 coefficients.

6.2 Mass variations in the Sahara Desert

We further conduct a similar analysis for validation areas in the Sahara Desert, another place with minimal mass variations. Validation areas in this region should allow us to check the quality of the tesseral coefficients, and in particular of C_{11} coefficient among the four estimated coefficients, as the surface spherical harmonic of degree 1 and order 0 reaches maximum in that area, exceeding the other three surface spherical harmonic under consideration.

In Fig. 13, we show the considered validation area (indicated with a red polygon in panel a). The resulting RMS value of the mass variation time-series based on various version of GRACE solutions are shown in panel b. This time, we notice that **SWEDeg1 + SLRC20** is able to reduce the RMS value by about 50 per cent. **INVDeg1 + SLRC20** and **CMBDeg1 + CMBC20** manage to further reduce the RMS estimates by about 0.1 cm. On the other hand, **SLRDeg1 + SLRC20** worsen the results significantly.

A clear seasonal pattern reveals itself in the mass variation time-series based on the **Ori GRC** (Fig 13c). Switching C_{20} coefficient between different variants barely changes the resultant seasonal pattern. This is expected because the zonal degree 2 surface spherical harmonic at the latitude of 22.5° is only 30 per cent of the values at the poles. Adding the degree-1 coefficients based on the GRACE-OBP-Swenson, joint inversion or the combination approach to the GRACE solutions reduces the annual amplitude of the seasonal pattern (Fig. 13d). When using the SLR-based degree-1 coefficients, we end up having an even more prominent seasonal pattern, which again, is in anti-phase with the original one.

6.3 Trend estimates in mass transport time-series

In Table 3, we show the linear trend estimates extracted from different mass transport time-series for both validation areas. Note that the GIA contributions are cleaned from all variants of the GRACE solutions, including both low- (degree-1 and C_{20}) and high-degree coefficients. Therefore, the obtained trend estimates should reflect the present-day mass transport rates. The large discrepancy between these trend estimates suggests the large uncertainty in GIA models (e.g. Klemann & Martinec 2011; A *et al.* 2012).

7 CONCLUSIONS AND DISCUSSION

We have developed a combination approach for a statistically optimal estimation of degree-1 and C_{20} coefficients. We have also shown that the combination approach is a generalization of the GRACE-OBP approach proposed by Swenson *et al.* (2008) and improved by Sun *et al.* (2016b). If GRACE data are free of noise, whereas noise
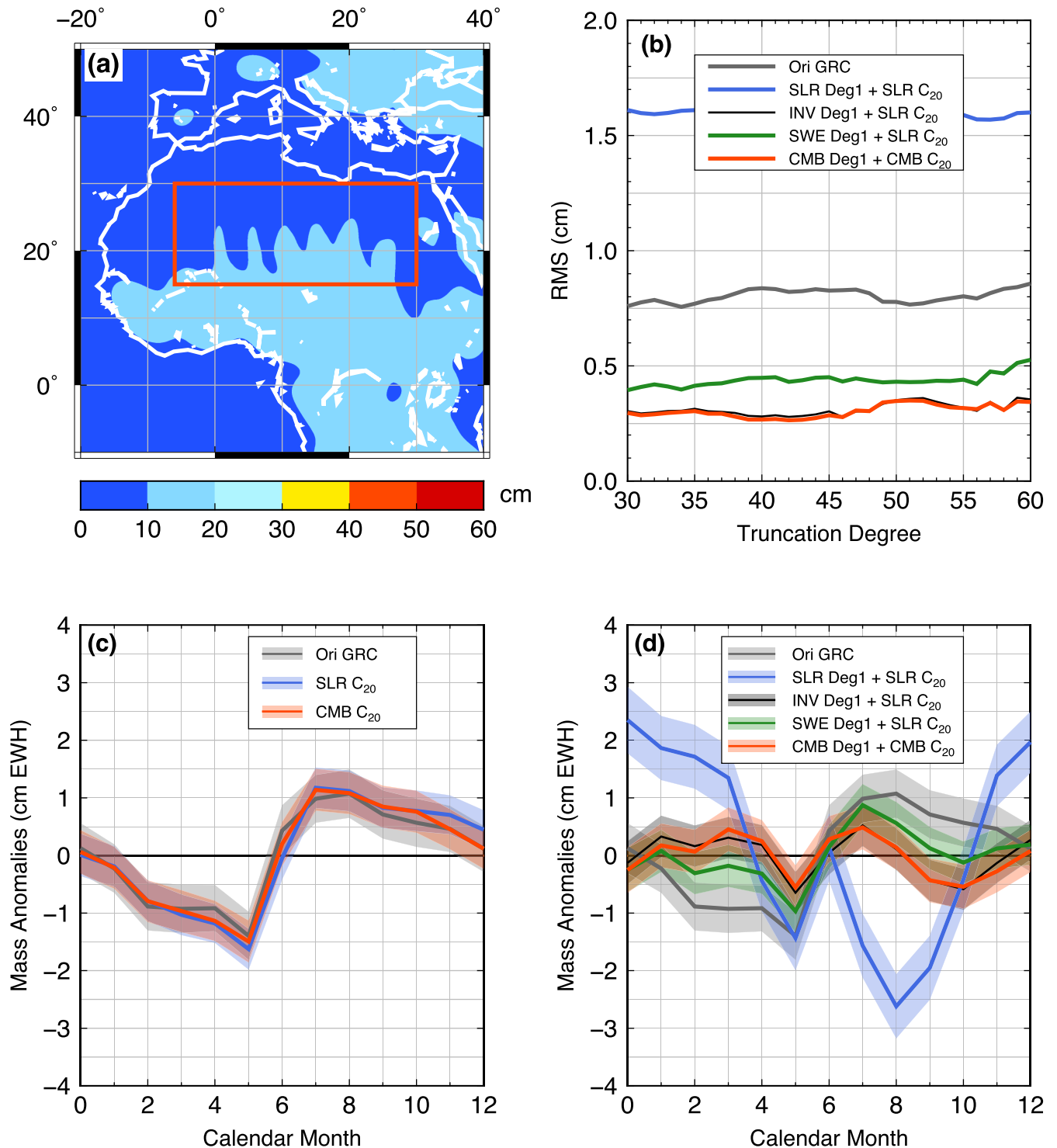
Figure 13. Same as Fig. 12, but showing mass transport in the validation area at the Sahara Desert (6°W/30°E/15°N/30°N).

in OBP data is white, then the combination approach reduces to the GRACE-OBP-Improved approach.

Based on the numerical experiments, we find that the overall quality of the resultant degree-1 and C_{20} time-series can be largely improved (RMS errors are reduced by about 30 per cent) by taking into account the stochastic information of noise in the input data sets. Degree-1 and C_{20} coefficients based on real data are then computed. The obtained annual variations are similar to those of other approaches. However, we do notice that the annual ampli-

tude of the SLR C_{10} time-series is about 1 mm larger than our estimates as well as many others. The annual phase of our C_{10} coefficients is more than a month later than the SLR- and GPS-derived solutions (Rietbroek *et al.* 2012; Cheng *et al.* 2013b; Wu *et al.* 2015) but close to the solution based on GRACE and altimetry data (Rietbroek *et al.* 2016). Error estimates and the correlation coefficients are also important product of the proposed approach. Remarkably, they are provided not as constant numbers, but as time-series.

Table 3. Estimates of linear trends in the resulting mass transport time-series (August 2002–June 2014). See Section 6 for the explanation of the names in the first column. Note that the degree-1 solution denoted by **INVDeg1**. These degree-1 coefficients are associated with surface load only and the modelled GIA signals are not restored. In the last two rows, we also show the results after restore GIA signals to the GRACE solutions.

GRACE solutions	East Antarctic (cm yr^{-1})	Sahara Desert (cm yr^{-1})
Ori GRC	-0.58 ± 0.06	0.11 ± 0.04
SWEDeg1 + SLRC20	0.00 ± 0.03	-0.10 ± 0.03
INVDeg1 + SLRC20	0.10 ± 0.03	-0.08 ± 0.03
GODeg1 + GOC20	-0.39 ± 0.03	0.05 ± 0.03
CMBDeg1 + CMBC20	-0.45 ± 0.03	0.11 ± 0.03
GODeg1 + GOC20 GIA restored	0.14 ± 0.03	0.04 ± 0.03
CMBDeg1 + CMBC20 GIA restored	0.08 ± 0.03	0.10 ± 0.03

To validate the resulting degree-1 and C_{20} coefficients, we selected two validation areas with minimal mass variations (central East Antarctica and Sahara Desert). Those areas are used to compare estimates of surface mass anomalies obtained from GRACE solutions corrected with 7 different combinations of degree-1 and C_{20} coefficients in estimating surface mass anomalies. It should be noted that the mass anomalies in the selected validation areas are relatively insensitive to the S_{11} coefficients. Fortunately, seasonal signals in the S_{11} time-series are the most consistent (among the three degree-1 coefficients) between the results from different techniques (Table 1). This is likely because the S_{11} coefficient (or the Y component of the geocentre motion), is well controlled by spatial variations of mass and gravity field at non-polar areas centred at 90° and 270° longitudes, and those areas are relatively well represented in the networks of both SLR and GPS stations.

Even though the annual amplitude of the C_{10} time-series based on Swenson *et al.* (2008) is reported to be small, it results in reasonable surface mass anomaly estimates. In contrast, the SLR-based degree-1 coefficients (Cheng *et al.* 2013b) are not sufficiently accurate for estimating surface mass anomalies. Probably, the annual amplitude is overestimated and the annual phase is wrongly estimated. This finding is consistent with the fact that SLR technique is relatively inaccurate in the estimation of the C_{10} and C_{11} coefficients SLR is inaccurate due to a poor quality of tropospheric corrections, too few ground stations in polar areas, and the absence of stations over oceans.

Contradictory to the numerical results, the degree-1 and C_{20} solution from the GRACE-OBP-Improved approach (**GODeg1 + GOC20**) performs slightly better (about 10 per cent) than that based on the proposed approach in terms of the resulting RMS values of the mass transport time-series. The reasons are still under investigation.

By switching from the C_{20} solutions based on the combination approach to those obtained with the SLR technique (while applying the same degree-1 solution based on the combination approach), we find a marginal difference (about 10 per cent) in the resultant RMS value of the mass transport time-series. This is an indication that our C_{20} time-series and the SLR-based one are of similar quality.

As far as the future developments are concerned, the combination approach will benefit from improvements in the input data sets. Future OBP models will likely be more accurate. More realistic covariance matrices for OBP noise will further enhance the advantage of this approach. In order to also address the linear trends in degree-1 and C_{20} coefficients, a better way of dealing with the solid Earth signals is warranted. Until now, those signals are accounted for with

a GIA model, which is assumed to be free of errors. However, large uncertainties in GIA modelling and the fact that tectonic signals are ignored (e.g. due to megathrust earthquakes) could substantially affect the trend estimates in the low-degree coefficients.

Finally, our products after taking into account the full error covariance matrices of the GRACE data and a more advanced error model for the OBP products are publicly available at http://www.citg.tudelft.nl/deg1c20).

REFERENCES

A, G., Wahr, J. & Zhong, S., 2012. Computations of the viscoelastic response of a 3-D compressible Earth to surface loading: an application to Glacial Isostatic Adjustment in Antarctica and Canada, *Geophys. J. Int.,* **192**(2), 557–572.

Bettadpur, S., 2012. UTCSR Level-2 Processing Standards Document., Technical Version 4, Univ. Texas, Austin.

Blewitt, G., 2003. Self-consistency in reference frames, geocenter definition, and surface loading of the solid Earth, *J. geophys. Res.,* **108**(B2), 2103, doi:10.1029/2002JB002082.

Chen, J.L., Wilson, C.R. & Ries, J.C., 2016. Broadband assessment of degree-2 gravitational changes from GRACE and other estimates, 2002–2015, *J. geophys. Res.,* **121**(3), 2112–2128.

Cheng, M. & Ries, J., 2017. The unexpected signal in GRACE estimates of C_{20}, *J. Geod.,* 1–18, in press, doi:10.1007/s00190-016-0995-5.

Cheng, M., Tapley, B.D. & Ries, J.C., 2013a. Deceleration in the Earth's oblateness, *J. geophys. Res.,* **118**(2), 740–747.

Cheng, M.K., Ries, J.C. & Tapley, B.D., 2013b. Geocenter variations from analysis of SLR data, in *Reference Frames for Applications in Geosciences,* no. 138 in International Association of Geodesy Symposia, pp. 19–25, eds Altamimi, Z. & Collilieux, X., Springer.

Conrad, C.P. & Hager, B.H., 1997. Spatial variations in the rate of sea level rise caused by the present-day melting of glaciers and ice sheets, *Geophys. Res. Lett.,* **24**(12), 1503–1506.

Dahle, C., Flechtner, F., Gruber, C., König, D., König, R., Michalak, G., Neumayer, K.-H. & GFZ, D.G., 2013. *GFZ GRACE Level-2 Processing Standards Document for Level-2 Product Release 0005,* Deutsches GeoForschungsZentrum GFZ.

Ditmar, P., Tangdamrongsub, N., Ran, J. & Klees, R., 2017. Mass anomaly time-series based on satellite gravimetry data: regularization and noise quantification, *Geophys. J. Int.,* submitted.

Dobslaw, H., Bergmann-Wolf, I., Dill, R., Forootan, E., Klemann, V., Kusche, J. & Sasgen, I., 2015. The updated ESA Earth System Model for future gravity mission simulation studies, *J. Geod.,* **89**(5), 505–513.

Dobslaw, H., Bergmann-Wolf, I., Forootan, E., Dahle, C., Mayer-Gürr, T., Kusche, J. & Flechtner, F., 2016. Modeling of present-day atmosphere and ocean non-tidal de-aliasing errors for future gravity mission simulations, *J. Geod.,* **90**(5), 423–436.

Dong, D., Fang, P., Bock, Y., Cheng, M.K. & Miyazaki, S., 2002. Anatomy of apparent seasonal variations from GPS-derived site position time series, *J. geophys. Res.,* **107**(B4), 2075, doi:10.1029/2001JB000573.

Farahani, H.H. *et al.*, 2017. A high resolution model of linear trend in mass variations from DMT-2: Added value of accounting for coloured noise in GRACE data, *J. Geodyn.,* **103,** 12–25.

Farrell, W.E. & Clark, J.A., 1976. On Postglacial Sea Level, *Geophys. J. R. astr. Soc.,* **46**(3), 647–667.

Flechtner, F. & Dobslaw, H., 2013. AOD1b Product Description Document for Product Release. 05, GFZ German Research Centre for Geosciences.

Gordeev, R.G., Kagan, B.A. & Polyakov, E.V., 1977. The effects of loading and self-attraction on global ocean tides: the model and the results of a numerical experiment, *J. Phys. Oceanogr.,* **7**(2), 161–170.

Griffiths, J. & Ray, J.R., 2013. Sub-daily alias and draconitic errors in the IGS orbits, *GPS Solut.,* **17**(3), 413–422.

Helsen, M.M. *et al.*, 2008. Elevation Changes in Antarctica Mainly Determined by Accumulation Variability, *Science,* **320**(5883), 1626–1629.

Jansen, M.J.F., Gunter, B.C. & Kusche, J., 2009. The impact of GRACE, GPS and OBP data on estimates of global mass redistribution, *Geophys. J. Int.,* **177**(1), 1–13.

Klemann, V. & Martinec, Z., 2011. Contribution of glacial-isostatic adjustment to the geocenter motion, *Tectonophysics,* **511**(3–4), 99–108.

Klinger, B. & Mayer-Gürr, T., 2016. The role of accelerometer data calibration within GRACE gravity field recovery: results from ITSG-Grace2016, *Adv. Space Res.,* **58**(9), 1597–1609.

Koch, K.-R. & Kusche, J., 2002. Regularization of geopotential determination from satellite data by variance components, *J. Geod.,* **76**(5), 259–268.

Kusche, J., Schmidt, R., Petrovic, S. & Rietbroek, R., 2009. Decorrelated GRACE time-variable gravity solutions by GFZ, and their validation using a hydrological model, *J. Geod.,* **83**(10), 903–913.

Lemoine, J.-M., Bruinsma, S., Gégout, P., Biancale, R. & Bourgogne, S., 2013. Release 3 of the GRACE gravity solutions from CNES/GRGS, vol. 15, pp. EGU2013–11123.

Liu, X., Ditmar, P., Siemes, C., Slobbe, D.C., Revtova, E., Klees, R., Riva, R. & Zhao, Q., 2010. DEOS Mass Transport model (DMT-1) based on GRACE satellite data: methodology and validation, *Geophys. J. Int.,* **181**(2), 769–788.

Mitrovica, J.X., Tamisiea, M.E., Davis, J.L. & Milne, G.A., 2001. Recent mass balance of polar ice sheets inferred from patterns of global sea-level change, *Nature,* **409**(6823), 1026–1029.

Ray, J., 1999. IERS Analysis Campaign to Investigate Motions of the Geocenter, Technical Note 25, Central Bureau of IERS Observatioire de Paris, Paris.

Ries, J.C., 2013. Annual Geocenter Motion from Space Geodesy and Models, in *AGU Fall Meeting Abstracts,* 1, 06.

Rietbroek, R., Brunnabend, S.-E., Dahle, C., Kusche, J., Flechtner, F., Schröter, J. & Timmermann, R., 2009. Changes in total ocean mass derived from GRACE, GPS, and ocean modeling with weekly resolution, *J. geophys. Res.,* **114**, C11004, doi:10.1029/2009JC005449

Rietbroek, R., Fritsche, M., Brunnabend, S.E., Daras, I., Kusche, J., Schröter, J., Flechtner, F. & Dietrich, R., 2012. Global surface mass from a new combination of GRACE, modelled OBP and reprocessed GPS data, *J. Geodyn.,* **59–60,** 64–71.

Rietbroek, R., Brunnabend, S.-E., Kusche, J., Schröter, J. & Dahle, C., 2016. Revisiting the contemporary sea-level budget on global and regional scales, *Proc. Natl. Acad. Sci. USA,* **113**(6), 1504–1509.

Sośnica, K., Thaller, D., Dach, R., Jäggi, A. & Beutler, G., 2013. Impact of loading displacements on SLR-derived parameters and on the consistency between GNSS and SLR results, *J. Geod.,* **87**(8), 751–769.

Sun, Y., Ditmar, P. & Riva, R., 2016a. Observed changes in the Earth's dynamic oblateness from GRACE data and geophysical models, *J. Geod.,* **90**(1), 81–89.

Sun, Y., Riva, R. & Ditmar, P., 2016b. Optimizing estimates of annual variations and trends in geocenter motion and J2 from a combination of GRACE data and geophysical models, *J. geophys. Res.*, **121**(11), 8352–8370.

Swenson, S., Chambers, D. & Wahr, J., 2008. Estimating geocenter variations from a combination of GRACE and ocean model output, *J. geophys. Res.,* **113**, B08410, doi:10.1029/2007JB005338.

Tamisiea, M.E., Hill, E.M., Ponte, R.M., Davis, J.L., Velicogna, I. & Vinogradova, N.T., 2010. Impact of self-attraction and loading on the annual cycle in sea level, *J. geophys. Res.,* **115**, C07004, doi:10.1029/2009JC005687.

Tapley, B.D., Bettadpur, S., Watkins, M. & Reigber, C., 2004. The gravity recovery and climate experiment: mission overview and early results, *Geophys. Res. Lett.,* **31**, L09607, doi:10.1029/2004GL019920.

Wahr, J., Molenaar, M. & Bryan, F., 1998. Time variability of the Earth's gravity field: hydrological and oceanic effects and their possible detection using GRACE, *J. geophys. Res.,* **103**(B12), 30 205–30 229.

Wahr, J., Nerem, R.S. & Bettadpur, S.V., 2015. The pole tide and its effect on GRACE time-variable gravity measurements: implications for estimates of surface mass variations, *J. geophys. Res.,* **120**(6), 4597–4615.

Watkins, M., 2012. JPL Level-2 Processing Standards Document, Technical Version 4, Jet Propulsion Laboratory.

Wu, X., Heflin, M.B., Ivins, E.R. & Fukumori, I., 2006. Seasonal and interannual global surface mass variations from multisatellite geodetic data, *J. geophys. Res.,* **111**, B09401, doi:10.1029/2005JB004100.

Wu, X., Ray, J. & van Dam, T., 2012. Geocenter motion and its geodetic and geophysical implications, *J. Geodyn.,* **58**, 44–61.

Wu, X. *et al.*, 2015. KALREF—A Kalman filter and time series approach to the International Terrestrial Reference Frame realization, *J. geophys. Res.,* **120**(5), 3775–3802.

APPENDIX A: GENERAL FORM OF DATA COMBINATION

$$\mathbf{d}_c = \left(\mathbf{A}_1^T \mathbf{C}_1^{-1} \mathbf{A}_1 + \mathbf{A}_2^T \mathbf{C}_2^{-1} \mathbf{A}_2 + \ldots + \mathbf{A}_n^T \mathbf{C}_n^{-1} \mathbf{A}_n \right)^{-1} \cdot$$

$$\left(\mathbf{A}_1^T \mathbf{C}_1^{-1} \mathbf{d}_1 + \mathbf{A}_2^T \mathbf{C}_2^{-1} \mathbf{d}_2 + \ldots + \mathbf{A}_n^T \mathbf{C}_n^{-1} \mathbf{d}_n \right), \tag{A1}$$

where $\mathbf{A}_1$, $\mathbf{A}_2$, $\ldots$, $\mathbf{A}_n$ are design matrices and $\mathbf{C}_1$, $\mathbf{C}_2$, $\ldots$, $\mathbf{C}_n$ are the noise variance-covariance matrices corresponding to data sets d_1, d_2, $\ldots$, d_n, respectively.

APPENDIX B: EXPLICIT FORM OF EQUATION (20)

In eq. (20), $\mathbf{Y}'$ is a $K \times 4$ matrix that can be written explicitly as

$$\mathbf{Y}' = \begin{bmatrix} P_{10}(\cos\theta_1) & P_{11}(\cos\theta_1)\cos\phi_1 & P_{11}(\cos\theta_1)\sin\phi_1 & P_{20}(\cos\theta_1) \\ P_{10}(\cos\theta_2) & P_{11}(\cos\theta_2)\cos\phi_2 & P_{11}(\cos\theta_2)\sin\phi_2 & P_{20}(\cos\theta_2) \\ \vdots & \vdots & \vdots & \vdots \\ P_{10}(\cos\theta_K) & P_{11}(\cos\theta_K)\cos\phi_K & P_{11}(\cos\theta_K)\sin\phi_K & P_{20}(\cos\theta_3) \end{bmatrix}, \tag{B1}$$

where θ and ϕ are the colatitude and longitude at point k, respectively.

Therefore, $\mathbf{Y}'^T\mathbf{O}\mathbf{Y}'$ becomes a 4×4 matrix

$$\mathbf{Y}'^T\mathbf{O}\mathbf{Y}' = \begin{bmatrix} I_{10C}^{10C} & I_{11C}^{10C} & I_{11S}^{10C} & I_{20C}^{10C} \\ I_{10C}^{11C} & I_{11C}^{11C} & I_{11S}^{11C} & I_{20C}^{11C} \\ I_{10C}^{11S} & I_{11C}^{11S} & I_{11S}^{11S} & I_{20C}^{11S} \\ I_{10C}^{20C} & I_{11C}^{20C} & I_{11S}^{20C} & I_{20C}^{20C} \end{bmatrix}, \tag{B2}$$

where, the following notation is used

$$I_{11C}^{10C} = \int d\Omega P_{10}(\cos\theta)\vartheta(\theta,\phi)P_{11}(\cos\theta)\cos\phi$$

$$I_{11S}^{11C} = \int d\Omega P_{11}(\cos\theta)\cos\phi\,\vartheta(\theta,\phi)P_{11}(\cos\theta)\sin\phi$$

Other elements are similarly defined. $\hspace{2cm}$ (B3)

Clearly, $\mathbf{Y}'^T\mathbf{O}\mathbf{h}$ is composed of the oceanic degree-1 and C_{20} coefficients C_{10}^{ocean}, C_{11}^{ocean}, S_{11}^{ocean} and C_{20}^{ocean}.

Finally, we have

$$\mathbf{Y}'^T\mathbf{O}\mathbf{h}_g = \begin{bmatrix} \int d\Omega P_{10}(\cos\theta)\vartheta(\theta,\phi)\mathbf{h}_g \\ \int d\Omega P_{11}(\cos\theta)\cos\phi\,\vartheta(\theta,\phi)\mathbf{h}_g \\ \int d\Omega P_{11}(\cos\theta)\sin\phi\,\vartheta(\theta,\phi)\mathbf{h}_g \\ \int d\Omega P_{20}(\cos\theta)\vartheta(\theta,\phi)\mathbf{h}_g \end{bmatrix} = \begin{bmatrix} -G_{10C} \\ -G_{11C} \\ -G_{11S} \\ -G_{20C} \end{bmatrix} \tag{B4}$$

APPENDIX C: BASIC IDEAS OF THE APPROACH BY DITMAR *ET AL.* (2017) FOR THE QUANTIFICATION OF RANDOM NOISE IN A DATA TIME-SERIES

That approach is based on the assumptions that (i) true signal in the data time-series is close (but not necessarily equal) to a combination of an annual periodic signal and a linear trend; (ii) noise in the time-series is uncorrelated and (optionally) non-stationary; (iii) time-series of noise variances is known up to a constant multiplier (scaling factor). Then, the data time-series is approximated by a regularized one on the basis of a properly designed regularization functional ($\Omega[H]$):

$$\Omega[H] = \sum_{k=1}^{K-1}(h_{k+1}(t) - h_k(t))^2 dt, \tag{C1}$$

where K is the total number of years considered and $h_k(t)$ is by definition the mass anomaly in the kth year; $h_{k+1}(0) = h_k(1)$ due to the continuity of $H(t)$.

The optimal regularization parameter is estimated with the Variance Component Estimation (VCE) technique (Koch & Kusche 2002), which includes the proper scaling of the provided noise variances. Then, the time-series of scaled noise variances is the measure of actual random noise in the considered data.